Referencing of Continental-Scale InSAR-Derived Velocity Fields: Case Study of the Eastern Tibetan Plateau

Laëtitia Lemrabet, Marie-pierre Doin, Cécile Lasserre, Philippe Durand

JGR Solid Earth

RESEARCH ARTICLE
10.1029/2022JB026251

Referencing of Continental-Scale InSAR-Derived Velocity Fields: Case Study of the Eastern Tibetan Plateau

Laëtitia Lemrabet[1], Marie-Pierre Doin[2], Cécile Lasserre[1], and Philippe Durand[3]

[1]Université de Lyon, UCBL, ENSL, CNRS, LGL-TPE, Villeurbanne, France, [2]ISTerre, University Grenoble Alpes, University Savoie Mont Blanc, CNRS, IRD, UGE, Grenoble, France, [3]Centre National d'Études Spatiales, Toulouse, France

Key Points:

- Phase ramps in Sentinel-1 interferograms are dominated by solid earth tides, seasonal signals and a linear term due to plate motion
- The simple tying of InSAR velocity maps in ITRF makes them mostly independent from GNSS data at large-scale, with an agreement of 1.4 mm/yr
- Horizontal and vertical velocity maps show interseismic motion and the effect of permafrost degradation and hydrologic fluctuations

Supporting Information:

Supporting Information may be found in the online version of this article.

Correspondence to:

M.-P. Doin,
marie-pierre.doin@univ-grenoble-alpes.fr

Citation:

Lemrabet, L., Doin, M.-P., Lasserre, C., & Durand, P. (2023). Referencing of continental-scale InSAR-derived velocity fields: Case study of the eastern Tibetan Plateau. *Journal of Geophysical Research: Solid Earth*, *128*, e2022JB026251. https://doi.org/10.1029/2022JB026251

Received 15 DEC 2022
Accepted 26 JUN 2023

Author Contributions:

Data curation: Philippe Durand
Formal analysis: Laëtitia Lemrabet, Marie-Pierre Doin, Cécile Lasserre
Funding acquisition: Marie-Pierre Doin, Cécile Lasserre
Investigation: Cécile Lasserre
Methodology: Laëtitia Lemrabet, Marie-Pierre Doin, Cécile Lasserre
Project Administration: Cécile Lasserre
Software: Laëtitia Lemrabet, Marie-Pierre Doin

Abstract The wealth of Sentinel-1 data in eastern Tibet allows to discuss whether InSAR-derived velocity maps measure ground motion in the ITRF reference frame with sufficient accuracy for large-scale tectonic applications. High elevation, moderate relief and low vegetation cover in eastern Tibet ensure reliable multi-temporal InSAR results. We automatically process seven 1,200 km long ascending and descending orbits, divided into 2 or 3 overlapping segments along-track. Linear phase ramps in range and azimuth are removed from interferograms. The ramps and the flattened interferograms are separately inverted into time series and analyzed. The ramps are modeled by their Solid Earth Tides (SET) contribution, seasonal variations, and a trend in time. SET oscillations are clearly visible in the ramp time series. Seasonal tidal amplifications of probable atmospheric origin are also evidenced. Ramp rates are shown to precisely quantify the plate motion of each segment in the ITRF reference frame. They are thus added back to the velocity maps before along-track merging. Then, a simple referencing procedure implying only a constant and a tilt in azimuth adjusted for each track is constrained by horizontal GNSS data. It allows straightforward vertical and horizontal decomposition. The quality of the merged and referenced data sets can then be quantitatively assessed at 1 mm/yr by the differences between InSAR and GNSS velocities and by the InSAR residuals on track overlaps. The vertical velocity field is dominated at first order by the effect of permafrost degradation, while the horizontal velocity highlights strain accumulation across major strike-slip faults in eastern Tibet.

Plain Language Summary The imagery acquired by the Sentinel-1 satellites allows to map the earth surface displacement field with an unprecedented resolution in space and time. The radar interferometric technique (InSAR) allows to form time-series of electromagnetic wave delays between the satellite and the ground for each pixel of the radar footprint. We here analyze in details the differential delay time series at very large scale, that is, between the east and western parts (250 km apart), or between the southern and northern parts (700 km apart) of 30 satellite footprints in Eastern Tibet. We show that this differential delays are explained by the displacements due to tides of the Solid Earth and due to plate tectonic drift with respect to the orbit reference frame. The robust analysis of the largest-scale delay measurements allows to tie the InSAR velocity measurements to a reference frame with a minimum input from GNSS observations. InSAR-GNSS velocity measurements can then be compared and show an agreement within 1.4 mm/yr. Velocity maps from ascending and descending tracks are combined to obtain horizontal and vertical velocities. The maps display clearly the interseismic motion on faults and the effect of permafrost degradation and interannual hydrological fluctuations.

1. Introduction

The ever-increasing temporal resolution and spatial coverage of radar interferometry (InSAR) satellite data has expanded the application fields of InSAR. For tectonic studies of active faulting and continental-scale deformation, the use of InSAR has gradually evolved from local-scale studies of earthquakes and fault seismic cycle (e.g., Bürgmann et al., 2000; Massonnet et al., 1993) to analyzes at the large-scale of major fault systems and plate-tectonics (e.g., Cavalié & Jónsson, 2014; Walters et al., 2014; H. Wang & Wright, 2012; Weiss et al., 2020).

InSAR time series analysis over longer and longer time spans contributed to improve our understanding of the mechanisms of postseismic deformation (e.g., Peltzer et al., 1996). It also made it possible to constrain not only the average rates of tectonic loading on faults at depth (e.g., Cavalié et al., 2008; Wright et al., 2001) but also the spatio-temporal evolution of slip in the seismogenic zone during the interseismic period (e.g., Jolivet et al., 2012, 2015; Maubant et al., 2020). Recent studies even highlight the interest of time series analysis for coseismic

Supervision: Marie-Pierre Doin, Cécile Lasserre
Validation: Laëtitia Lemrabet, Marie-Pierre Doin, Cécile Lasserre
Writing – original draft: Laëtitia Lemrabet, Marie-Pierre Doin, Cécile Lasserre
Writing – review & editing: Philippe Durand

studies to improve the signal-to-noise ratio and complete near-field data (Grandin et al., 2017; Liu et al., 2021; Marconato et al., 2022). However, large-scale perturbations after earthquakes and long-distance interactions between faults, with possible long time delays, have been observed from geodesy (e.g., Durand et al., 2010; Trubienko et al., 2013). They now require to enlarge the study of surface deformation associated with the seismic cycle to a continental scale. For InSAR measurements, this in turn requires to reconsider the methods for their referencing and discuss their potential for measuring plate tectonic motion in global reference frame systems (e.g., Parizzi et al., 2021; Stephenson et al., 2022; Xu & Sandwell, 2020). The issues of disentangling the tectonic signal from the non-tectonic signal and separating the horizontal and vertical movements from all signal sources are also at stake (e.g., Daout et al., 2017, 2020; Hu et al., 2021).

With these new goals in sight, the launch of the Sentinel-1 (S1) satellites in 2014 and 2016 has opened a new era for surface deformation observations, providing open access to a large volume of data, acquired systematically at the global scale over large areas (including high seismic hazard regions) at unprecedented temporal resolution. Exploitation of the first years of S1 data has already demonstrated, still focusing on the example of tectonics, the ability of such a dense data set both to detect tiny aseismic transient events along faults (e.g., Aslan et al., 2019) and to quantify strain partitioning and localization in the interaction zones of tectonic plates (e.g., Moore et al., 2021; Weiss et al., 2020).

InSAR measurements are differences in time of phases measured with a 2π ambiguity on the satellite to ground distance and as such are relative measurements in time and space. The uncertainty of these relative measurements increases significantly with distance (Parizzi et al., 2021). Indeed, the large spatial wavelengths in InSAR displacement or velocity maps remain affected by uncorrected phase contributions due to the atmosphere (tropospheric or ionospheric delays), inaccurate orbital information, solid earth tide effects (Xu & Sandwell, 2020) or other atmospheric, hydrologic or oceanic tidal loading (DiCaprio & Simons, 2008; Yu et al., 2020). Absolute referencing and displacement mapping at large-scale therefore classically requires a combination with Global Navigation Satellite System (GNSS) measurements. Several methods exist to express InSAR and GNSS data in a common reference frame. They are generally based on the assumption that the GNSS reference sites to which the InSAR data will be tied have negligible relative vertical motion. Only a few GNSS points can be selected for referencing InSAR data (e.g., Li et al., 2022), preferably in areas of low vertical signal and low noise level for both geodetic data sets, or dense GNSS networks can be used depending on the studied area. To fit GNSS data, linear or quadratic polynomial functions in both range and azimuth directions can be added to InSAR velocity maps (e.g., Hussain et al., 2018; Walters et al., 2014; Weiss et al., 2020). Alternatively, for a more isotropic referencing procedure, a first-order low-pass GNSS-based velocity model, projected into the Line Of Sight, (LOS) can be removed from the InSAR velocity maps, then the residuals are high-pass filtered and the GNSS-based model is added back (e.g., Lanari et al., 2020; Tong et al., 2013; Wei et al., 2010). This is done for each frame individually, before merging. The GNSS-based model may be interpolated from velocity measurements at GNSS sites after a robust outlier removal procedure (Lanari et al., 2020), or may derive from modeled displacement fields constrained by GNSS data after an inversion (Tong et al., 2013). The key parameter is the cutoff wavelength of the high-pass filter applied to the residual InSAR velocity maps after GNSS correction. The GNSS-based field must be complete and accurate for all wavelengths down to the cutoff wavelength in the whole area of interest, as discussed in Tong et al. (2013). The InSAR (referenced or not) and GNSS data can be jointly inverted to retrieve a 2D-3D velocity field model at large scale, although this implies data down-sampling and regularization by spatial smoothing (e.g., Walters et al., 2014; H. Wang & Wright, 2012). Alternatively, an east-west and up/down decomposition of the InSAR referenced velocity field can be computed using both ascending and descending viewing geometries, often neglecting north-south motion (see Brouwer & Hanssen, 2021).

In this paper, we tackle this issue of InSAR data referencing, testing a new approach limiting dependence on GNSS data, with the specific objective of retrieving surface deformation at the continental-scale in an International Terrestrial Reference Frame (ITRF) (Altamimi et al., 2012). This approach is suitable for new generation InSAR satellites such as Sentinel-1 (S1) with improved orbit accuracy. We develop and validate it based on a large set of InSAR velocity maps and time series products from the FLATSIM service (ForM@Ter LArge-scale multi-Temporal Sentinel-1 InterferoMetry, Thollard et al., 2021) over the eastern Tibetan plateau. The study area is of $\simeq$1,300 km $\times$ 1,300 km, covered by 14 tracks along descending and ascending orbits (Figure 1). This region is marked by major thrusts and strike-slip fault systems with high seismic hazard, which kinematics and slip behavior have been monitored by InSAR since the ERS generation (e.g., Cavalié et al., 2008; Jolivet et al., 2012; H. Wang & Wright, 2012; Ou et al., 2022). Being part of the highest and widest plateau on Earth, it

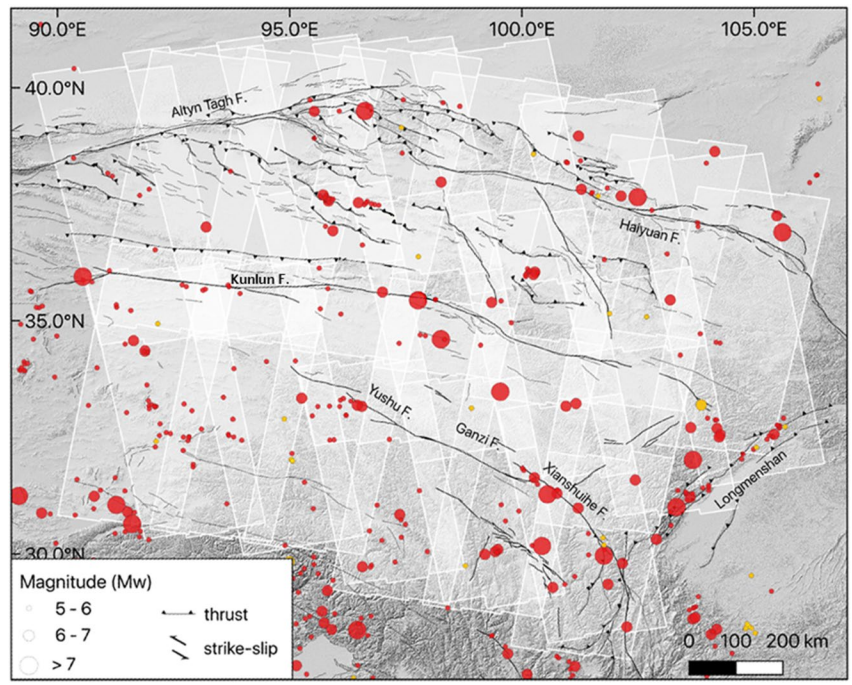

Figure 1. Seismotectonic map of the eastern part of the Tibetan plateau superimposed on the shaded SRTM digital elevation model (Farr et al., 2007). Black lines represent major active faults from Tapponnier and Molnar (1977). Red circles indicate major earthquakes from the International Seismological Centre (1904–1983) and National Earthquake Information Center (1984–2022) catalogs. Yellow circles represents the seismicity during the InSAR acquisition period for this study (2014–2020). Sentinel-1 track locations are overprinted in light gray.

has long been studied to debate on the mechanisms of continental deformation (Clark & Royden, 2000; England & Jackson, 1989; Tapponnier et al., 1990). There is also a growing interest in the region for non tectonic processes such as permafrost seasonal fluctuations and long-term degradation (Daout et al., 2017, 2020). S1 acquisitions are available over the Tibetan plateau every 24 days (S1-A) to 12 days (with the added capacity of S1-B), providing a data set with unprecedented resolution for methodological advances (this study) and further analysis of tectonic and non-tectonic processes (out of scope of the current paper).

We first present the FLATSIM products used in this study, highlighting their specificities with respect to previous work and their particular interest in terms of processing to improve InSAR referencing for large-scale studies. We then perform a time series analysis of the phase ramps in range and azimuth estimated in the original interferograms by the FLATSIM service, discuss the contributions of solid earth tides on these and if/how accurate the ramp rates are to describe plate motion in an ITRF reference frame. Finally, we propose a methodology for merging InSAR velocity maps from different tracks in such a reference frame system, requiring a separation of linear velocity terms from seasonal variations and a limited adjustment to GNSS data. We provide at the end unique InSAR LOS velocity fields over the eastern Tibetan plateau in both ascending and descending orbit geometries, showing an agreement with GNSS data at a 1 mm/yr level in LOS. A decomposition into horizontal and vertical motion further validates the approach and highlights the potential for future analysis of deformation processes.

2. Massive Automated InSAR Processing Over Eastern Tibet

2.1. InSAR Data Set and FLATSIM Products

FLATSIM is a ForM@Ter service operated by the french spatial agency, CNES (Centre National d'Etudes Spatiales), aiming to systematically produce interferograms and time-series analyzes from Sentinel-1 data, over large geographic areas (Thollard et al., 2021). It is based on the InSAR New Small temporal and spatial BASelines processing chain (NSBAS) (Doin et al., 2011; Grandin, 2015). Here, we use Sentinel-1A/B radar images acquired in the Interferometric Wide (IW) Swath mode, along 7 ascending and 7 descending orbits from October 2014 to October 2020 (see Table S1 in Supporting Information S1). Data are processed by 600–700 km long

track segments, each of them covering on average 30 to 35 bursts, and overlapping by at least 150 km along the azimuthal direction (Figure 1 and Figure S1 in Supporting Information S1). This strategy differs from that of other automated services, such as LICSAR (Lazecký et al., 2020) and ARIA (Bekaert et al., 2019), which process approximately 8 bursts' chunks. The advantage of processing long segments is that it improves certain processing steps, as for example, the coregistration step or the unwrapping step (by getting around low coherence areas), or the retrieval of spectral diversity parameters and of phase offsets between subswaths (see subsection below). It also provides a consistent solution throughout the segment. The process of merging all track segments is also simplified and facilitated by the large overlapping region. The FLATSIM service provides wrapped or unwrapped, filtered or raw interferograms in terrain or radar geometry. Besides the result of the time series inversion of the unwrapped interferometric network, it also gives many useful auxiliary data sets to validate the automated processing and, if necessary, to re-process certain track segments.

2.2. Processing Details in Relation to the Retrieval of Large-Scale Motion

We describe below some specificities of the FLATSIM processing steps, that are relevant to our large-scale study and the understanding of all post-processing analyzes. We refer to Thollard et al. (2021) for more details.

1. The first processing step is carried out separately on the three sub-swaths of the radar images (the same for steps 2 to 5). We select the range of bursts to process for each track segment that falls between the user-defined maximum and minimum latitudes. Incomplete acquisitions, that is, with missing bursts in the burst range, are excluded from the data set. Depending on the track segment, 84 to 142 acquisition dates are selected (Table S1 in Supporting Information S1).
2. A central reference image is chosen for each track segment. We then use the 1 arc-second Shuttle Radar Topography Mission digital elevation model (DEM) (Farr et al., 2007) and the orbit of the reference acquisition to simulate a radar backscatter intensity image and the surface elevation in the geometry of the reference image.
3. All Single Look Complex (SLC) images are then built by assembling bursts and removing the antenna steering function from the phase. Precise orbits are taken from the Copernicus Precise Orbit Determination (CPOD) service (Peter et al., 2017) in early 2021, before their complete reprocessing in a homogeneous framework (Fernández et al., 2022). The SLC coregistration on the reference image is then performed in successive steps. First, the precise orbits and the DEM are used to simulate the distortion field in range between the reference and secondary images. Then, image correlation is used to refine this first estimate, adding a constant offset in range to this simulated field and an affine function of range and azimuth for the distortion field in azimuth. The distortion fields are used to resample the secondary SLCs into the reference geometry. Note that the empirical offset in range accounts for a possible translation velocity of the secondary SLCs with respect to the reference SLC due to absolute plate motion in the orbit reference frame, but does not affect the interferometric phase.
4. The interferometric network is built from the pairing of successive acquisitions ($n/n + 1$), each acquisition n with its next plus two ($n/n + 2$), each acquisition n with its next plus three ($n/n + 3$), then from systematic pairing of images two to 3 months apart and about 1 year apart with a reduced perpendicular baseline. The number of differential interferograms per track segment varies between 353 and 665 (Table S1 in Supporting Information S1), of which about one sixth have a temporal baseline longer than 10 months.
5. Differential backward-forward interferograms are computed over the successive burst overlapping areas (about 30 overlaps for our data set) to extract the Enhanced Spectral Diversity (ESD) phase (Prats-Iraola et al., 2012). This ESD phase is fitted by a constant, a bilinear ramp in range and azimuth, and a constant gradient within burst overlaps. These four ESD fit parameters are inverted into time series to improve their reliability and avoid a drift with time that could result from accumulating random errors. Such network inversion of the ESD phase is also performed by Fattahi et al. (2017) to stabilize the ESD retrieval over long time series. After inversion of the ESD parameters, they are used to correct interferograms with a sawtooth function modulated in range and azimuth and a corrugated (by burst) sheet function. The auxiliary data provided by the FLATSIM service have been checked during the validation procedure to verify that the ESD inversion process for all these parameters is stable and that the ESD parameters are of very good quality for each acquisition. Along-track motion affects the ESD phase but is not a component of the interferometric phase.
6. At this stage, the interferograms obtained for each sub-swath separately, multilooked by a factor of 8 in range and 2 in azimuth, are merged using the annotations provided with the SLC data. A phase offset between contiguous sub-swaths and per acquisition is computed by inverting the phase offsets measured on the interferograms' overlaps between sub-swaths. It is then applied to avoid phase jumps between sub-swaths. The quality of the time series of the inverted phase offsets is also checked for each track segment.

7. This step and the next ones (atmospheric correction, filtering, unwrapping) are applied using procedures already developed for ERS or Envisat data (Daout et al., 2018; Doin et al., 2015). Interferograms are corrected from tropospheric delay predictions by the ERA5 model provided by the European Center for Medium-Range Weather Forecasts (ECMWF) (Doin et al., 2009; Jolivet et al., 2011) and then multi-looked to 32 in range and 8 in azimuth. Low-pass filtering is applied using a sliding window. Interferograms are unwrapped by a coherence-based region-growing algorithm described in Grandin et al. (2012), starting from an automatically selected point in an area of high coherence. Interferograms with low unwrapping fractions are automatically discarded.
8. Linear phase ramps in range, a_{ij}, and azimuth, b_{ij}, in mm/km, are estimated for each interferogram between dates i and j, using an iterative procedure eliminating outliers, by adjusting:

$$\phi_{ij}(x, y) = \frac{4\pi}{\lambda}(a_{ij}\beta x + b_{ij} y + c + r_{ij}(x, y)), \quad (1)$$

   where $\phi_{ij}(x, y)$ is the unwrapped phase in radian and positive away from satellite, λ is the radar wavelength, x is the satellite to ground range in km, $\beta = 1/\sin(\theta_m)$ is a constant scaling factor to transform range in approximate ground distance with $\theta_m = 33.9°$, and y the azimuth in km, c is a constant and $r_{ij}(x, y)$ is the residual, zero-mean, phase. The standard deviation, σ_{ij}, of the residual phase is also estimated for each interferogram.
9. These ramps a_{ij} and b_{ij} are inverted in time series to retrieve at each time step k the ramp coefficients a^o_k and b^o_k, in mm/km, and the residual phase standard deviation, σ^{APS}_k (Biggs et al., 2007; Cavalié et al., 2007), with an iteration to down-weight outliers. The σ^{APS}_k values represent the mean Atmospheric Phase Screen (APS) amplitude of each acquisition (Doin et al., 2011). The inverted ramp coefficients are used to correct (or "flatten") interferograms. Interferograms with particularly large standard deviations are automatically discarded, ensuring the rejection of anomalous acquisitions that may exist at the beginning of the time series.
10. Finally, filtered, unwrapped, flattened interferograms are referenced to a small area located around the unwrapping seed point and inverted into displacement time series, with an automatic correction of unwrapping errors (Doin et al., 2011, 2015; Ho Tong Minh et al., 2022; López-Quiroz et al., 2009). Network misclosures, averaged by date or by interferogram, are all checked during the validation procedure of the FLATSIM products.

Some quality maps are provided by FLATSIM (Thollard et al., 2021). Among them, the root mean square (RMS) misclosure maps, describing the residual during interferometric network inversion, are displayed in Figure S2 in Supporting Information S1 for each processed track. They quantify the quality of the unwrapping step. We consider that the RMS should be less than 0.5 radians to ensure good quality. Two segments (D150S and A070S, Figures S1 and S2 in Supporting Information S1) exhibit large network misclosure values. They correspond to unwrapping errors acquired when crossing basins subject to strong deformation gradients due to freeze-thaw cycles (Daout et al., 2017). For tracks A099S and A055 (Figure S1 in Supporting Information S1), located in the easternmost area with steep relief, the unwrapped FLATSIM interferograms were re-inverted into time series after changing the reference area and eliminating interferograms with large unwrapping errors.

The Line Of Sight (LOS) velocity maps produced by FLATSIM (or slightly post-processed for some tracks as mentioned above) for ascending and descending track segments are shown in Figure 2 (a constant offset is added to each velocity map to improve the readability of the figures). Note that, although almost fully automatic, the processing described above still produce high quality velocity maps.

In the following, we separately analyze the inverted time series from the phase ramps (Sections 3 and 4) and the FLATSIM flattened interferograms (Section 5), as summarized in the flowchart displayed in Figure 3. We show that InSAR phase ramps in range and azimuth measure the oscillations of solid earth tides quite well, and some other tidal oscillations probably of atmospheric origin. We then explore the accuracy of the ramps' trends with time (hereafter referred to as ramp rates) and show that the estimated ramp rates are accurate enough for being re-introduced in the FLATSIM flattened velocity maps. We also present the reasons for a separate ramp analysis, mainly how it optimizes its retrieval and how it leads to an uncertainty estimation.

3. Tidal Oscillations Observed in Time Series of InSAR Phase Ramps

3.1. Contribution of Solid Earth Tides on InSAR Ramps and Modeling

Solid Earth tides (SET) are known to affect the interferometric phase and are included in the Sentinel-1 Extended Timing Annotation Datasets (S1 ETAD) in the geodetic correction set (Eineder et al., 2015). As shown in

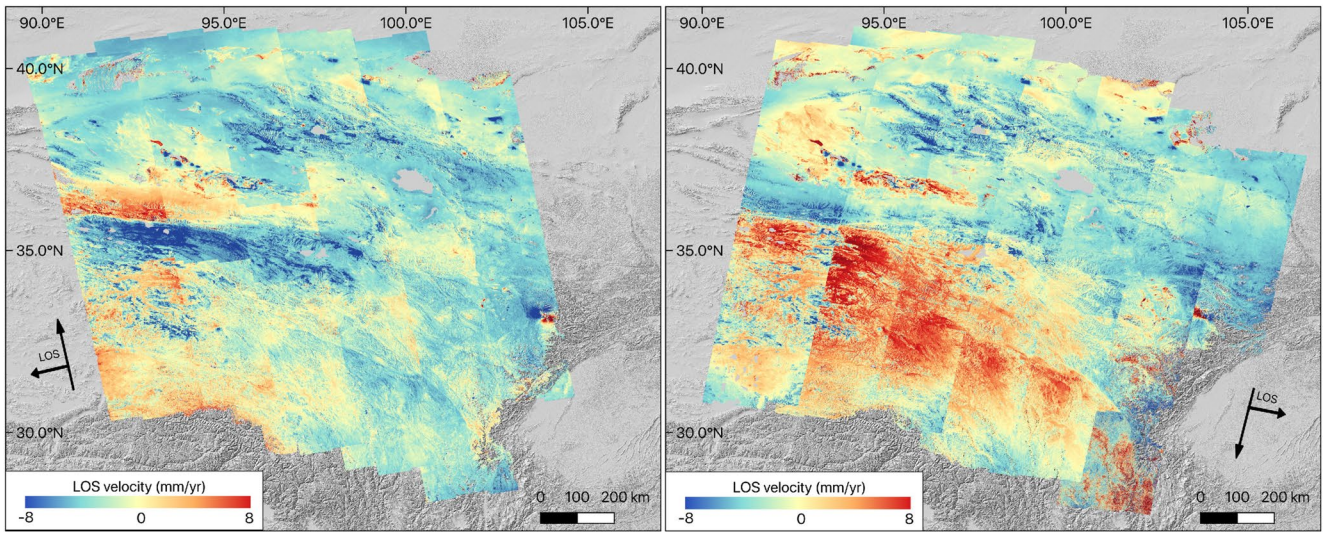

Figure 2. Line of sight velocity maps (corrected from linear phase ramps, see details in text) from automated FLATSIM processing, with an offset manually added to each track segment to improve figure readability. Left panel: ascending geometry. Right panel: descending geometry. Positive and negative values indicate ground motion toward and away from satellite, respectively. The velocity map for D135S (southeasternmost track in the right panel) is altered by a 1.25 years data gap.

Figure 4a, their main contribution is a phase ramp in range due to the vertical surface displacement (Xu & Sandwell, 2020). As the S1 incidence angle varies from 29° in near range to 46° in far range, a uniform peak to peak vertical displacement, U_{SET}, of 280 mm (as produced by SET in Tibet) yields a LOS range change of U_{SET}*cos(29°) = 240 mm in near range and of U_{SET}*cos(46°) = 190 mm in far range (Xu & Sandwell, 2020), thus a peak to peak ramp change in range of about 0.20 mm/km. In addition, SET also induce a very large scale deformation pattern, with wavelengths of the order of ten thousand kilometers. The small displacement gradient in range adds to the preceding contribution, but is one order of magnitude smaller. In azimuth, both the displacement gradient and the evolving tide during the acquisition period (1–2 min) produce a small phase ramp in azimuth (Figure 4c), which is peak to peak of the order of 0.02 mm/km in Tibet. The phase ramps in range and azimuth due to SET oscillate in time with the characteristic periods of tides.

In order to compare ramp observations from InSAR with SET-induced ramps, then correct them, we run forward models of SET using the numerical code of V. Dehant and modified by D. Milbert, which defines SET in IERS 2003 convention (McCarthy & Petit, 2004) for spherical harmonic degrees 2 and 3. Displacements are computed for each acquisition date of our InSAR time series on radar footprints. We convert the predicted surface displacement field (horizontal and vertical components) in LOS range change, yielding at each time step, k, the predicted ramp in range, a_k^t, and azimuth, b_k^t.

3.2. Comparison Between Modeled and Observed InSAR Ramps in Range

We compare, for the 30 track segments in eastern Tibet and each time step, such predicted ramps in range, a_k^t, (in mm/km) with the observed ones, a_k^o, derived from the time series inversion of individual ramps in FLATSIM interferograms (see point 8 in Section 2.2 and Figure 3). The given error bar on observed ramps, $\sigma_{a_k}^o$, is the root mean square of the network misclosures between inverted, $\left(a_j^o - a_i^o\right)$, and measured, a_{ij}^o, ramps, for all interferometric pairs including a specific date, k:

$$\sigma_{a_k}^o = \left(\frac{1}{N^k} \sum_{\substack{i,j \\ \text{for } i=k \text{ or } j=k}} \left(a_o^j - a_o^i - a_o^{ij}\right)^2 \right)^{1/2}, \quad (2)$$

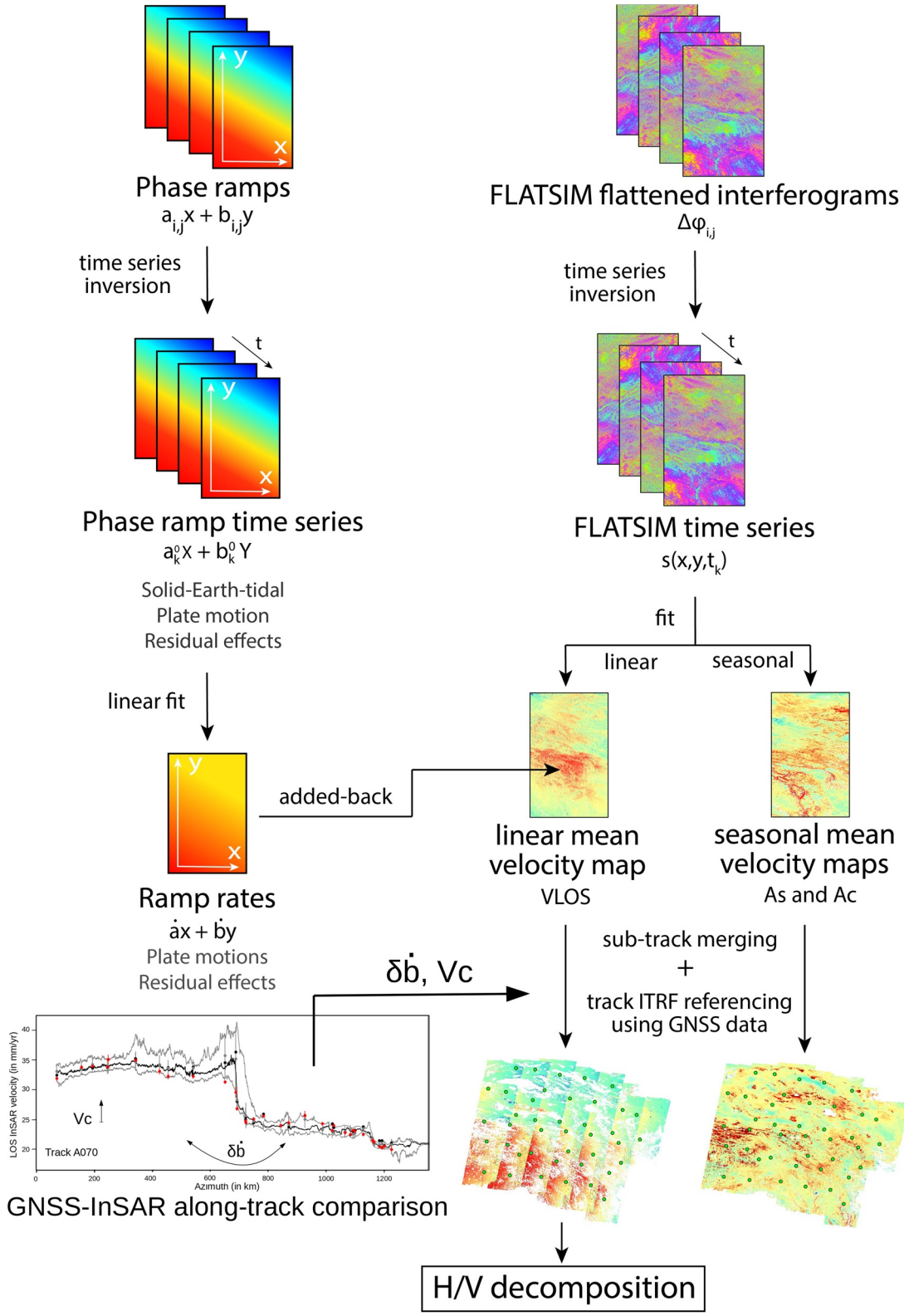

Figure 3. Sketch summarizing the processing steps performed in this study. Both the ramps (left column) and the FLATSIM flattened interferograms (right columns) are processed separately through temporal inversions for, respectively, a ramp rates analysis and the extraction of seasonal and linear signals from time series. Ramp rates are reintroduced before merging and referencing. A velocity offset, *Vc*, and a ramp in azimuth, $\delta\dot{b}$, estimated by GNSS-InSAR comparison on track-wide profile, are used for referencing each track.

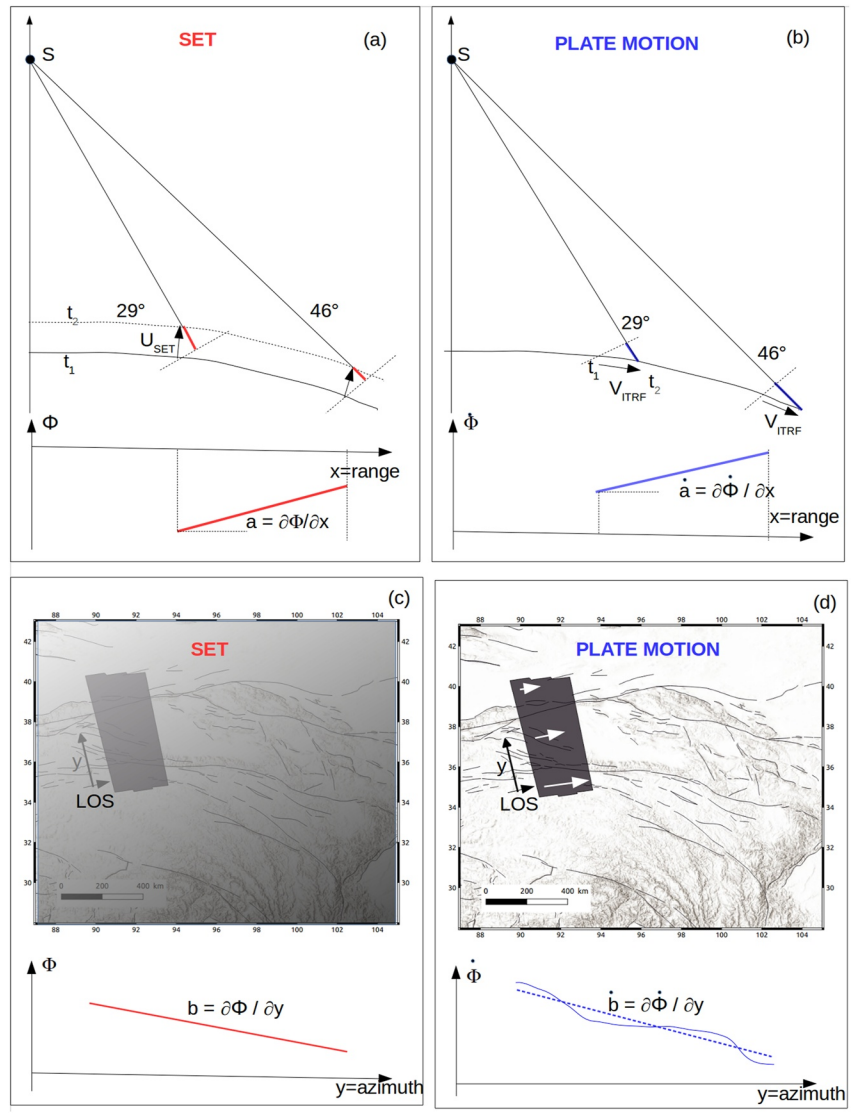

Figure 4. Sketch of the effect of solid earth tides (SET, panels a, c) and plate velocity in the ITRF orbit reference frame (panels b, d), on ramps in range (panels a, b) and azimuth (panels c, d). Panel (a): U_{SET} depicts the almost uniform vertical surface displacement between two dates t_1 and t_2 due to SET. Its projected effect on the satellite-ground distance and thus the phase ϕ, shown with red lines, varies with the local look angle. a is the ramp in range x resulting from the interferometric phase ϕ variation with range x. Panel (b): as panel (a) but for a uniform horizontal velocity drift, V_{ITRF}, of the plate in the orbit reference frame. The projected satellite-to-ground distance change is shown with blue lines and depends on the local look angle. $\dot{\phi}$ is the phase rate per unit time, and $\dot{a}$ is the ramp rate with range. Panel (c) shows the effect of a large-scale surface displacement field between two dates due to SET (gray gradients) across the satellite footprint (gray rectangle). It results in a small phase ramp b with azimuth y. Panel (d) shows the effect of an along-track variation of plate motion (white arrows) in the orbit reference frame. The along-track variation of $\dot{\phi}$ (blue solid line), which presents localization across faults, is fitted by a linear trend (blue dotted line) which defines a ramp rate $\dot{b}$ in azimuth. Phase delays are defined along the Line of Sight and are positive away from satellite. Modified from Xu and Sandwell (2020).

where N_k is the number of pairs containing the image k. It is a reconstruction error, assumed to quantify how well defined are the ramps on interferograms including a given date. An example of comparison between observed and predicted ramps is shown in Figure 5a for a descending track. Another example for an ascending track is shown in Supporting Information S1 (Figure S3a).

The agreement between the observed and predicted phase ramps in range is striking. Both time series present the same high frequency oscillations that correspond to the aliasing of the tide frequencies at the sampling of Sentinel-1 data. After removing the modeled tide ramps, the residual shows a clear trend and a seasonal

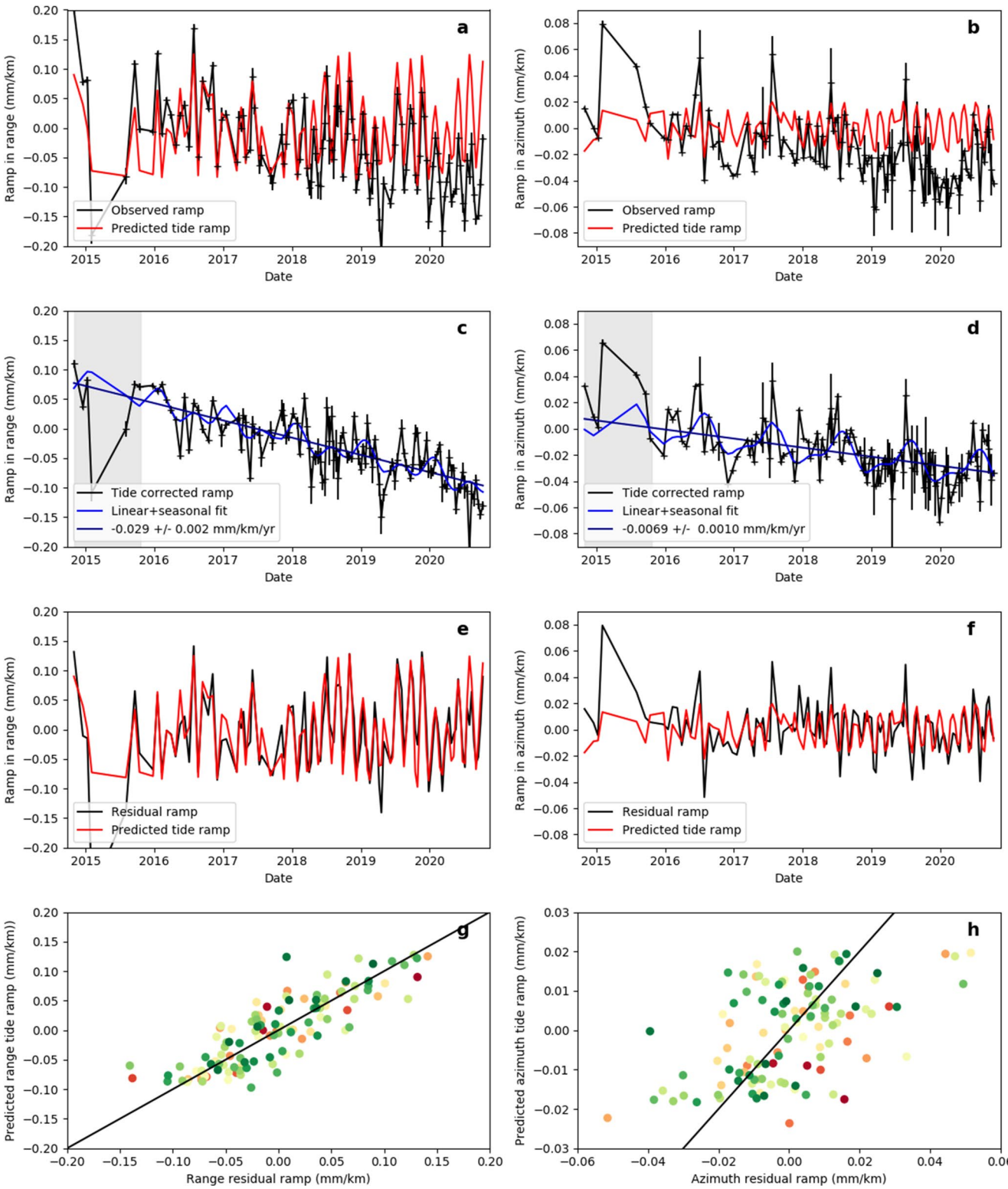

Figure 5. Analysis of ramps as a function of time for the northern segment of track D004. Panels (a, c, e, g) ramps in range. Panels (b, d, f, h) ramps in azimuth. Panels (a, b) Observed ramps at each time step, a_k^o or b_k^o, inverted from those measured on individual interferograms (black line), with their associated reconstruction uncertainties, $\sigma_{a_k}^o$ or $\sigma_{b_k}^o$ (crosses). Predicted ramps, a_k^t or b_k^t, due to solid earth tides (red line). Panels (c-d): Observed ramps corrected from tidal effect (black) together with the adjusted linear and seasonal fit (blue). Data in the gray area have a very low weight in the adjustment. Panels (e-f) Observed ramps after subtracting seasonal and linear fit (black), compared to predicted tidal ramps (red). Panels (g, h) as panels (e, f) but the predicted tidal ramps are shown as a function of residual ramps (from e, f), with a color scale varying from red for the earliest dates to dark green for the latest dates.

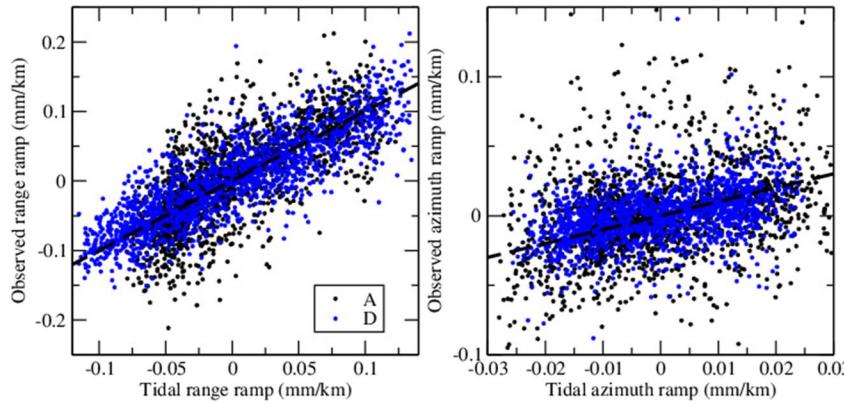

Figure 6. Observed ramps corrected from seasonal and linear trend versus predicted tidal ramps, for the whole data set, (a) in range, (b) in azimuth. Only dates later than 2016.8 (2015.8, respectively) are shown with black points for ascending tracks, A, (with blue dots for descending tracks, D, respectively).

oscillation (Figures 5c and 5e and Figures S3c, S3e of Supporting Information S1). Observed ramps in range are thus fitted using:

$$a_k^o = a_k^t + a_0 + \dot{a}\,t_k + a_c\cos(2\pi t_k) + a_s\sin(2\pi t_k) + a_{2c}\cos(4\pi t_k) + a_{2s}\sin(4\pi t_k) + \epsilon_a(t_k) \quad (3)$$

where t_k is the acquisition date in year, a_0 is a constant, $\dot{a}$ is the estimated ramp rate in range (in mm/km/yr), a_c and a_s are the amplitude of the cosine (winter–summer) and sine (spring–autumn) seasonal ramp variations, a_{2c} and a_{2s} are the amplitude of semi-seasonal ramp variations, and ϵ_a is the residual ramp. The fit is obtained by linear least square adjustment with a weight on each acquisition inversely proportional to the reconstruction uncertainty, $\sigma^o_{a_k}$, on a^o_k. To account for the presence of outliers in the time series, six iterations are performed by decreasing the weight of outliers. After removal of the linear and seasonal fit, the agreement between the observed and modeled ramps is even more striking (Figures 5e and 5g), both in the amplitude and timing of the tide oscillations.

The ramps in range shown for the ascending orbit example in Figure S3 in Supporting Information S1 are noisier. However, the high frequency oscillations of the ramps are clearly of tidal origin. The linear increase of the ramps in range with time, and the seasonal fluctuation are also evident. The agreement between the observed ramps, after removing the linear and seasonal fit, and the tidal prediction is summarized in Figure 6a. The root mean square residue of Equation 3, noted σ_a, is lower for descending tracks (σ_a = 0.042 mm/km) than for ascending tracks (σ_a = 0.050 mm/km).

3.3. Comparison Between Modeled and Observed InSAR Ramps in Azimuth

SET can also produce a non negligible ramp in the interferometric phase along the azimuth direction. However, this ramp is proportional to the latitudinal gradient of the SET-induced surface displacement, which is very low as SET displacement patterns are mostly significant up to spherical harmonic degree 3. This is why the ramp in azimuth due to SET has never, to our knowledge, been convincingly observed with InSAR.

Figure 5 and Figure S3 of Supporting Information S1 show two examples of time series of the observed $\left(b^o_k\right)$ and predicted $\left(b^t_k\right)$ ramps in azimuth as a function of time (panels b). Note that the amplitude of b^o_k variations (±0.015 mm/km) is at least four times smaller than that of the a^o_k variations (±0.10 mm/km). However, the 700 km-long InSAR chunks allow to measure phase gradients along azimuth with a relatively good accuracy. As in subsection 3.2, the ramps are adjusted by a constant, b_0, a linear trend, $\dot{b}$, and seasonal and semi-seasonal components with amplitudes b_c, b_s, b_{2c} and b_{2s} (panels d):

$$b^o_k = b^t_k + b_0 + \dot{b}t_k + b_c\cos(2\pi t_k) + b_s\sin(2\pi t_k) + b_{2c}\cos(4\pi t_k) + b_{2s}\sin(4\pi t_k) + \epsilon_b(t_k). \quad (4)$$

As for Equation 3, Equation 4 is weighted by the reconstruction uncertainties, $\sigma^o_{b_k}$, on b^o_k, and solved iteratively to decrease the impact of outliers. After removal of the fitted function of time, the oscillations of the residual ramp show a clear agreement with those of the predicted tidal ramp (panels f). The one to one comparison between

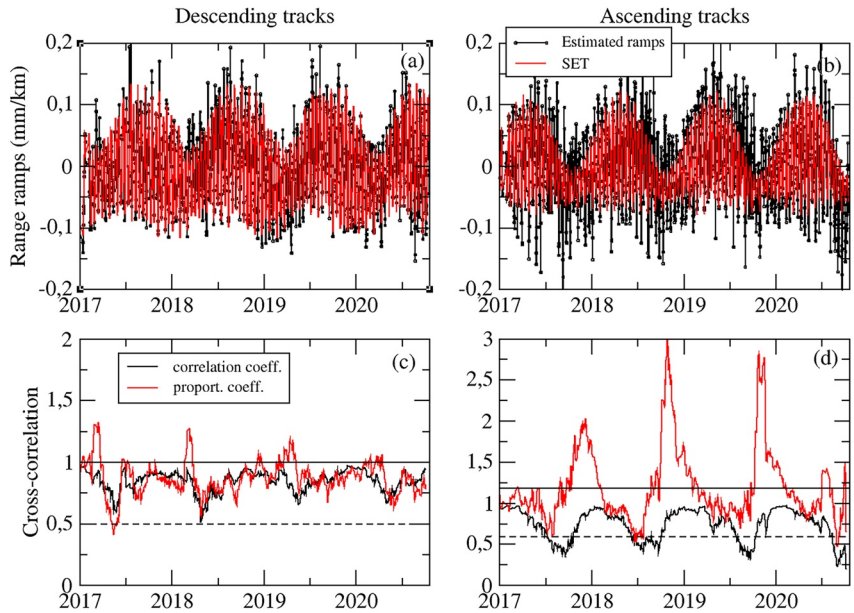

Figure 7. Temporal evolution of the correlation between observed InSAR ramps in range and SET predictions. (a, b) Predicted ramps in range (red line) and observed ramps corrected from seasonal and linear trend (black line and symbols), plotted as a function of time for descending (a) or ascending (b) tracks. (c, d) Correlation coefficient (ρ, black line) and regression slope (s, red line) obtained between observation and prediction on a moving window, covering two times the aliased SET cycle. Data before 2017 are noisier and not shown.

observed ramps, corrected from trend and seasonality, and predicted tidal ramps is shown in panels h, and for all tracks together in Figure 6b. The root mean square residue of Equation 4, noted σ_b, shows again, a slightly better agreement for descending tracks (σ_b = 0.020 mm/km) than for ascending tracks (σ_b = 0.029 mm/km), with less outliers.

3.4. Spectral Tide Identification in Ramp Time Series

In order to examine which tides can be identified above the noise level in the ramp time series, we collate all observations for the 30 InSAR track chunks, corrected from the trend and seasonal function, on two plots for descending and ascending tracks separately (Figures 7a and 7b for ramps in range and Figures S4a and S4b in Supporting Information S1 for ramps in azimuth). The sampling of the new time series is irregular (mainly 1, 2 or 3 days, or a few minutes between segments of a single track) but allows to display higher frequency oscillations than for a single track. We perform Lamb-Scargle periodograms on observed and modeled SET time series and display the amplitude of periods between 6 and 500 days (Figure 8 for ramps in range and Figure S5 in Supporting Information S1 for ramps in azimuth). Aliasing of tides, sampled as described above, is complex, as shown by the periodograms of modeled SET time series. However, it is dominated by the aliased periods of tides sampled at constant solar time (see Xu & Sandwell, 2020). The M2 (aliased at 14.765 days), O1 (aliased at 14.192 days), and even N2 (aliased at 9.614 days) tides are clearly above noise level in the time series of the ramp in range for the two orbit directions, and in the ramp in azimuth for descending data. Only M2 tide can be identified in the ramp in azimuth for the ascending data. The K1 and P1 tides, aliased with a period of about a year, are also present but the resolution of the periodograms at these frequencies is lower, and these tides are mixed with other seasonal contributions. Finally, in ascending data sets only, oscillations with periods of about 24 days stand above the noise level and may correspond to ionospheric perturbations.

3.5. Intriguing Observation of Apparent Seasonal Tidal Amplification

In Figures 5e, 5f and Figures S3e, S3f in Supporting Information S1, the tidal oscillations of InSAR ramps in range or azimuth, respectively, appear as if they were sometimes amplified compared to the predicted SET oscillations. However, a possible amplification effect cannot be assessed from the data of a single track. We

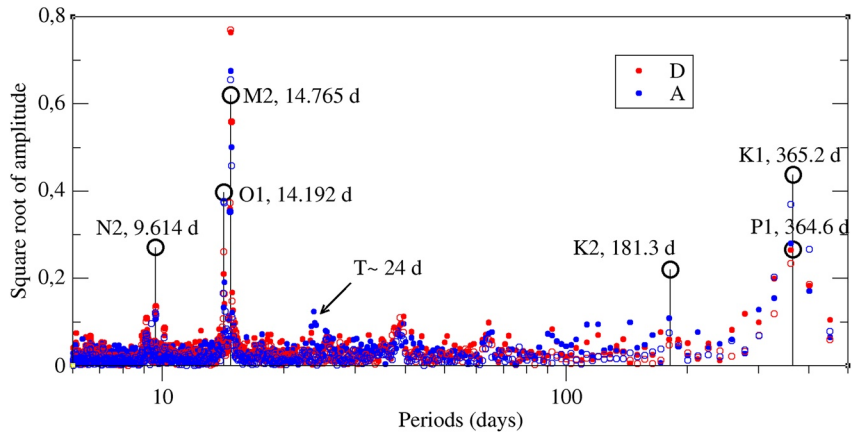

Figure 8. Lamb-Scargle periodogram for periods between 6 and 500 days (logarithmic scale) of observed (filled circles) and modeled (open circles) SET time series of the ramp in range. The analysis is performed separately for descending (red) and ascending (blue) tracks. The periods of the main tidal constituents, aliased by a sampling at a constant solar time, are shown with an open black circle and black vertical lines. A square root on amplitudes is applied to decrease the contrasts between the peaks.

use the collated observed and modeled ramp oscillations displayed in Figures 7a, 7b and Figures S4a, S4b in Supporting Information S1 to test possible tide amplifications. The time series are dominated by the 14.765 lunar semi-diurnal M2 oscillation, but modulated by the other tides. We perform a correlation between the SET predictions and the observed InSAR ramps on a moving window covering two times the aliased SET cycle. The correlation coefficient $\rho(t)$ and the regression slope, $s(t)$, are then examined as a function of time (Figures 7c and 7d for ramps in range and Figures S4c, S4d in Supporting Information S1 for ramps in azimuth). Values $\rho = 1$ and $s = 1$ would correspond to a perfect fit between the observations and the SET predictions. In the presence of white noise, without other tidal effects, we expect a concomitant and proportional variation of both ρ and s. Departure of the $s(t)$ curve from the $\rho(t)$ curve is thus indicative, for correlation coefficients larger than about 0.4, of tidal effects not taken into account in the SET prediction.

For the ramps in range (Figure 7), the variation of $\rho(t)$ is seasonal. It is mostly associated with variations in $s(t)$ for descending tracks, whereas $s(t)$ departs strongly from $\rho(t)$ for ascending tracks. On morning, descending tracks, we note short pulses of apparent tide amplification in winter months (February–March) of years 2017, 2018, and less significantly of years 2019 and 2020. Apparent tide amplification on late-afternoon, ascending tracks is much more pronounced and last longer, occurring from July to November, with more noise in July–August than in autumn months. Zooms of the 2018 tide amplification events are displayed on Figure 9. The contrast between tidal amplifications in ascending and descending tracks favors an atmospheric origin for these tidal effects. One possible origin is the semi-diurnal lunar ionospheric tides that affect the Total Electronic Content (TEC) (Pedatella & Forbes, 2010). The February–March amplifications might for example, be related to sudden stratospheric warming events (e.g., Forbes & Zhang, 2012). Temporal variations in the amplitude of M2 ionospheric tides of about 5 TEC units have also been reported by Paulino et al. (2021) in Brazil. Another origin might be the tropospheric lunar tides, that have a seasonal modulation but with a rather low amplitude (Kohyama & Wallace, 2014) or an orbit error of variable amplitude and correlated with tides. Given the level of aliasing in the time series, we cannot also exclude that the apparent tide amplification results from the combination with an oscillation with another frequency. Hence, although we favor a ionospheric origin, we are not aware of a direct observation proving the origin of the strong tidal oscillations observed in summer periods for ascending tracks only.

The ramps in azimuth are larger and noisier for ascending tracks than for descending tracks (Figure S4 in Supporting Information S1), with maximum amplitude in summer times. The correlation coefficients remain significant for descending tracks, and a clear seasonal tidal amplification can also be observed from June to October. Surprisingly, apparent amplifications in the ramp in azimuth are not concomitant to those in range. A zoom in 2019 (Figure S6 in Supporting Information S1) shows that despite noise, the period around 15 days is very clear in the data, especially after applying a 5-point sliding median. The amplification appears to result from a few large ramp values, positive or negative, however in phase with tidal oscillations. Similarly, the zoom in 2020 displayed for ascending tracks again shows large ramp values in phase with tidal oscillations.

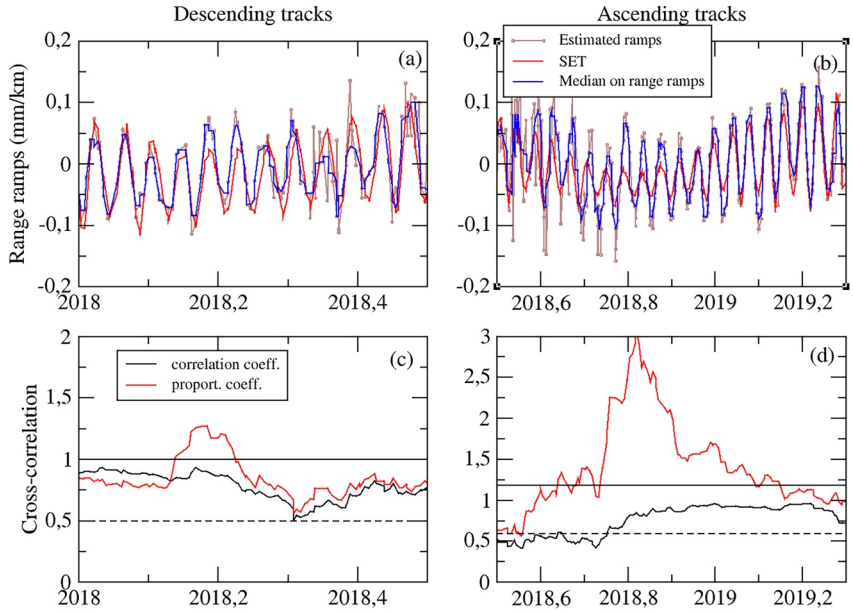

Figure 9. As Figure 7 but zooming on amplification events in 2018. On panels (a–b), observed ramps are drawn with gray lines and symbols, while a 5-data-wide sliding median is shown with a blue curve. SET predicted ramps are shown in red. For the noisier ascending track ramps, the median allows to better visualize the tidal oscillations in the data.

4. InSAR Ramp Rate: An Effect of Plate Motion in ITRF Reference Frame

4.1. Origin of InSAR Ramp Rates

GNSS data over the Tibetan plateau show an eastward motion in the ITRF reference frame, with eastward velocities of about 30–50 mm/yr, as shown Figure S9 in Supporting Information S1 (e.g., M. Wang & Shen, 2020). On InSAR time series for S1 tracks, a uniform plate velocity in the ITRF reference frame, V_{ITRF}, will produce, because of the look angle variation across the 250 km-wide track range (Figure 4b), a ramp rate in range of about V_{ITRF}*(sin(46°) − sin(29°))/250, that is, approximately 0.028–0.047 mm/km/yr. A gradient in range of the plate velocity within the satellite footprint will yield an additional, but in general smaller, ramp rate in range that will add up to the preceding contribution. Similarly, velocity gradients in azimuth, resulting for example, in Tibet from differential motion across E-W strike-slip faults, will produce a ramp rate in azimuth, as shown in Figure 4d. The ramp rates in azimuth, of the order of 0.01 mm/km/yr are smaller than the ramp rates in range. In order to test the hypothesis that the ramp rates we measured from our InSAR time series ($\dot{a}$ and $\dot{b}$ in Equations 3 and 4, respectively) are representative of plate motion in an ITRF reference frame, we first estimate their uncertainty, then compare the measured ramp rates with predicted values based on the GNSS velocity field.

4.2. Uncertainties on InSAR Ramp Rates in Range and Azimuth

The large number of acquisitions processed in this study over 14 tracks divided into 30 chunks allows to constrain the uncertainties due to measurement errors and unmodeled phenomena. The residual ramps, after correction from temporally correlated terms (trend and seasonal) and solid-earth tides, provide a quantification of uncorrelated noise due to unmodeled signals (residual tidal effects, large-scale ionospheric or tropospheric effects, orbital errors or atmospheric loading) or measurements errors. A residual ramp in range of ±0.042 mm/km (for descending tracks, see Section 3.2) corresponds to ±10 mm of relative displacement in LOS between far range and near range, whereas a residual ramp in azimuth of ±0.020 mm/km (for descending tracks, see Section 3.3) corresponds to ±20 mm of relative displacement in LOS for two points 1,000 km apart.

We derive from Equation 3 or 4 and the root mean square residuals, σ_a or σ_b, an uncertainty on the estimated InSAR ramp rate in range, $\sigma_{\dot{a}}$, or in azimuth, $\sigma_{\dot{b}}$, as:

$$\sigma_{\dot{a}} = \frac{\sigma_a}{\sqrt{N - 6}\sigma_t}, \quad (5)$$

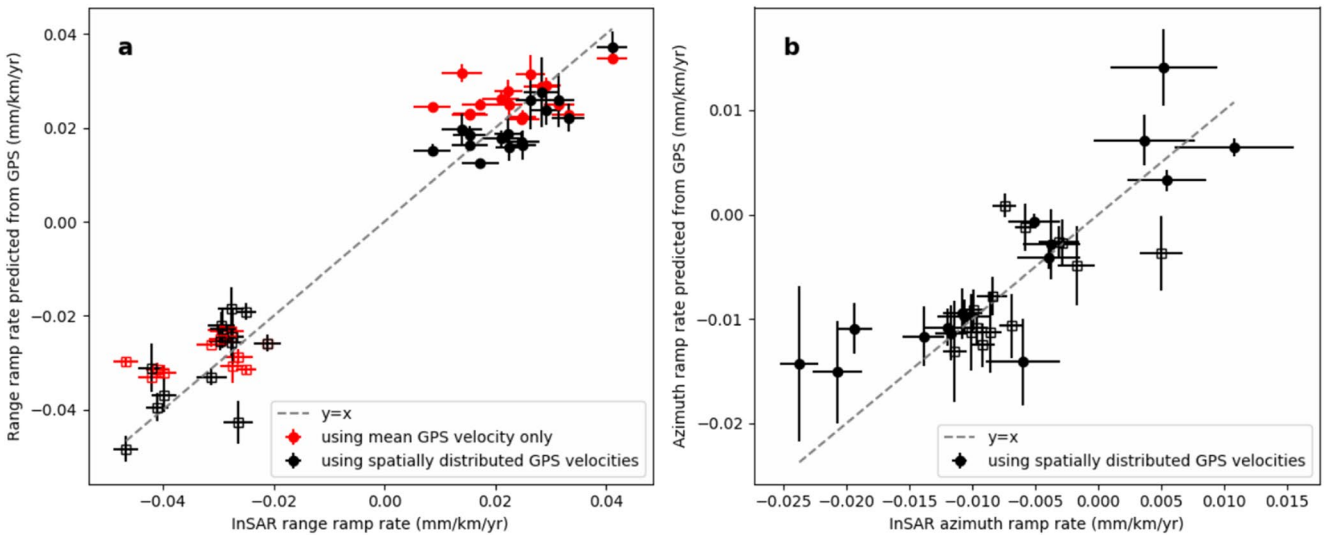

Figure 10. Comparison between InSAR-derived and GNSS predicted ramp rates, along LOS, (a) along the range direction, (b) along the azimuth direction. GNSS ramp rates are computed by a linear regression in azimuth and range of all horizontal GPS velocities in ITRF2008 available within each track segment (M. Wang & Shen, 2020) and projected into the LOS (black symbols with 1-σ error bar). Open squares: descending tracks, filled circles: ascending tracks. Red symbols correspond to the average ramp rate within each track segment, computed using the averaged GNSS velocity of all GNSS points located within the track and considering only the effect of varying incidence angle from near range to far range.

$$\sigma_{\dot{b}} = \frac{\sigma_b}{\sqrt{N-7}\sigma_t}, \tag{6}$$

where N is the number of acquisitions, $N-6$, the degree of freedom of Equation 2, and σ_t is the standard deviation of the acquisition times. The mean value of $\sigma_{\dot{a}}$ is 0.0030 mm/km/yr for ascending tracks and 0.0023 mm/km/yr for descending tracks. Despite large outliers (Figure S4 in Supporting Information S1) and a significant seasonal component, the ramp rate in azimuth is also relatively well constrained, with a mean value of $\sigma_{\dot{b}}$ of 0.0026 mm/km/yr for ascending tracks and of 0.0011 mm/km/yr for descending tracks. These values correspond on average to a differential velocity uncertainty of 0.65 mm/yr between near range and far range (250 km apart), and of about 1.9 mm/yr for two points 1,000 km apart in azimuth.

4.3. Comparison Between GNSS Predicted and InSAR Observed Ramp Rates

Here, we compare the InSAR ramp rates we inverted (Sections 3.2 and 3.3) with the prediction obtained from GNSS data, for each of the 30 available chunks in eastern Tibet. To do so, we assume that the large-scale surface displacement is purely horizontal. We use GNSS horizontal velocities, v_g^H, from M. Wang and Shen (2020), given in the ITRF 2008 reference frame. Within each track segment, we project them along the LOS using the local LOS unit vector to get v_g^{LOS}. We further assume that the sampling of GNSS data is dense and representative enough (see GNSS point locations in Figure S8 in Supporting Information S1) to adequately capture the average velocity and its average tilt in range and in azimuth that InSAR would measure in the LOS within each chunk.

We note $\bar{v}_g^H$ the average horizontal velocity per chunk obtained after weighting individual GNSS measurements by their given standard deviation, and after an iterative removal of the main outliers. The averaged tilt rate in range produced by this average surface velocity, $\dot{a}_g^m$, is the LOS projection from near range to far range of $\bar{v}_g^H$. The values of $\dot{a}_g^m$ are compared to the $\dot{a}$ values estimated from InSAR time series on Figure 10a (red symbols) for all chunks in ascending and descending geometries. The good agreement between the InSAR-derived values (positive $\dot{a}$ values of about 0.03 mm/km/yr observed for ascending tracks and negative $\dot{a}$ values of about −0.03 mm/km/yr for descending tracks) and GNSS-predicted ones shows that the ramp rates measured by InSAR are primarily due to the mean horizontal surface motion within InSAR chunks in the ITRF reference frame.

To further refine this analysis, taking into account horizontal gradients of the surface velocities within each chunk, we also adjust the GNSS velocities projected on LOS by:

$$v_g^{LOS} = \dot{a}_g x_g + \dot{b}_g y_g + c_g \tag{7}$$

where x_g and y_g are the range and azimuth of GNSS points, $\dot{a}_g$ is the estimated ramp rate in range using horizontal GNSS data and $\dot{b}_g$ is the estimated ramp rate in azimuth. The least-square adjustment is performed with a weight on each GNSS data proportional to its given standard deviation converted into LOS. Note that the GNSS data distribution in the westernmost tracks (rather along N-S profiles, Figure S8 in Supporting Information S1) does not necessarily allow an accurate separation between the ramp in range and the one in azimuth. Approximate 1-σ uncertainties, $\sigma_{\dot{a}_g}$ and $\sigma_{\dot{b}_g}$, are also estimated from Equation 7 using the residual GNSS LOS velocities and the degree of freedom.

The comparison between the ramp rates predicted from the spatially distributed GNSS data and those estimated with InSAR is shown with black symbols on Figure 10. We now observe for the ramp rate in range a better alignment within each ascending or descending point clouds (Figure 10a), except for one track. Similarly, a good agreement is also observed for the ramp rate in azimuth (Figure 10b). Importantly, no large bias on the ramp rates, that is, no large offset from the $y = x$ line, is observed. Deviations from the $x = y$ line in Figure 10 are also probably at least equally due to the large uncertainty in the GNSS-derived values of $\dot{a}_g$ and $\dot{b}_g$ than to the uncertainty on the InSAR-derived values $\dot{a}$ and $\dot{b}$. Indeed, we obtain quite large one-sigma standard deviations on $\dot{a}_g$ and $\dot{b}_g$ (Figure 10) due to uneven GNSS data quality (campaign or continuous stations) and uneven sampling (Figure S8 in Supporting Information S1). Furthermore, GNSS velocities do not sample the exact same period of the seismic cycle than InSAR data, and are corrected from post-seismic motion (M. Wang & Shen, 2020) in contrast with InSAR data. Finally, the asymmetric spatial sampling of GNSS data on either side of a fault, for example, will lead to differences with InSAR derived ramp rates. This is particularly true for ramps in azimuth, as large strike-slip faults in Tibet generate strong along-track gradients in LOS velocity, that are unevenly sampled by GNSS.

All this considered, the agreement shown on Figure 10, for ramp rates in range but also for ramps in azimuth, is quite remarkable and shows the potential of InSAR data to directly measure large-scale plate motion in the ITRF reference frame.

To summarize, we show that InSAR-measured ramp rates are dominated by large-scale tectonic plate motion, with uncertainties that have been quantified. In the following section, we therefore reintroduce the validated ramp rates in range and azimuth in velocity maps, after separating the linear trend and the seasonal signals from the FLATSIM time series, as shown in the flowchart displayed in Figure 3. We propose a simple methodology to merge and reference InSAR velocity maps of all tracks in the ITRF and further compare InSAR velocities extracted at GNSS data location and GNSS velocities projected into LOS.

5. Merging InSAR Velocity Maps at Large-Scale in the ITRF Reference Frame

5.1. Separation of Average Velocity and Seasonal Signals in FLATSIM Time Series

We first model the ground displacement, inverting the phase timeseries, $s(x, y, t_k)$, given by the FLATSIM service, for each pixel (x, y), to optimize the separation of the seasonal and linear ground movements. We model the ground displacement by:

$$s_m(x, y, t_k) = A_0(x, y) + A_c(x, y)\cos(2\pi t_k) + A_s(x, y)\sin(2\pi t_k) + V_{LOS}(x, y)(t_k - t_0) \tag{8}$$

where A_0, A_c and A_s correspond to a constant, the cosine (winter-summer) and sine (spring-autumn) amplitude of the seasonal displacement, respectively, V_{LOS} is the ground LOS velocity, and t_k is the acquisition time in year. t_0 is an arbitrary value taken at the beginning of the time-series. The least square estimation of the variables A_0, A_c, A_s and V_{LOS}, is weighted by $W(x, y, t_k)$ that depends on each pixel and on each acquisition, in order to take into account the fact that some acquisitions have large APS, defined by σ_{APS}, or large RMS misclosure, defined by σ_m, and that some values in the time series are large outliers. Furthermore, during

the iterative process, we redefine the reference area $s_{ref}(t_k)$ of each acquisition. For track segment D135S, as already mentioned before, a data gap of 1.2 years from 2017/03/08 to 2018/06/19 led to erroneous phase linking across the gap; another unknown variable proportional to a step across the data hole was therefore added in Equation 8.

We thus minimize the cost C:

$$C = \sum_{x,y,t_k} W(x,y,t_k)^2 * (s(x,y,t_k) - s_{ref}(t_k) - s_m(x,y,t_k))^2 \tag{9}$$

with

$$W(x,y,t_k) = \frac{1}{(\sigma_{APS}(t_k) + \epsilon) * (\max(\sigma_m(t_k), \epsilon)) * (|r(x,y,t_k)| + \epsilon)} \tag{10}$$

where $r(x, y, t_k) = s(x, y, t_k) - s_{ref}(t_k) - s_m(x, y, t_k)$ is the residue, σ_m is the mean of the root mean square network misclosure of all interferograms containing a given date t_k (López-Quiroz et al., 2009), $\sigma_{APS}(t_k)$ is the RMS of the residue for a given date (Doin et al., 2011), and ϵ is equal to 0.4 rad. The weighting in σ_m, constant for all iterations, is introduced to handle the cases where one or a few acquisitions have fringe patterns that systematically produce large unwrapping errors, as is for example, regularly observed in case of partial snow cover. When this happens, the automatic unwrapping error correction implemented in the NSBAS inversion scheme (Doin et al., 2011) fails. One inner loop of three iterations, made on a single pixel (x, y), allows to define the weight based on the residue $|r(x, y, t_k)|$. The outer loop, made of three iterations, is performed once all pixels have been processed in order to compute $\sigma_{APS}(t_k)$, and the reference value for each date, $s_{ref}(t_k)$, such that the average over a reference area of the residue $r(x, y, t_k)$ will be zero.

The reference area first covers the whole track segment. However, in a second step, it is restricted to the bedrock as in Daout et al. (2017), that is, to the area not affected by seasonal deformation of hydrological origin or due to permafrost freeze-thaw cycles. In order to automatically define the bedrock pixels, we analyze the along-track profiles of the term $A_s(x, y)$ of Equation 8, as shown in Figure S7 in Supporting Information S1. An along-profile large-wavelength fit is adjusted to the median values per each azimuth bin. This fit serves as a reference to mask pixels far from the fit line, affected by large seasonal signal. We chose the seasonal spring-autumn sine component to define bedrock as it is less affected by residual atmospheric delays than the winter-summer cosine term.

Figure 11 displays the resulting merged amplitude maps in the LOS of the spring-autumn signal (A_s in sine term of Equation 8) and of the winter-summer (A_c in cosine term of Equation 8) signal. The maps for each segment are simply juxtaposed without any offset adjustment. They are very consistent on tracks overlaps and for ascending and descending tracks, suggesting that they mostly represent well-defined vertical displacement signals. Uplift in spring and subsidence in winter is generalized over the highest elevation areas of the eastern Tibetan plateau. These signals, very pronounced on the sine maps, correspond to the effect of freeze-thaw cycles in permafrost areas, as described in Daout et al. (2017, 2020), and occur mainly within permafrost prone areas (T. Wang et al., 2020). Other hydrological signals are also apparent in both the cosine and sine maps, especially within catchment basins or at the foothills of mountains ranges in desert areas. The cosine maps also display strong residual tropospheric delays with pronounced phase-elevation relationships in deeply incised valleys of southeastern Tibet where the ERA-5 atmospheric correction is not accurate (Mathey et al., 2022). An in-depth analysis of the seasonal pattern is beyond the scope of the present paper.

For merging and referencing steps in the following, we use the average velocity maps (linear trend) extracted from Equation 8.

5.2. Merging InSAR Velocity Maps and Referencing in ITRF

The strategy proposed in this study aims to provide a regional InSAR velocity map that is as least constrained as possible by GNSS data, that is, using as few as possible degrees of freedom to put each InSAR velocity map in the ITRF2008 reference frame. This way, GNSS and InSAR data can still be viewed as independent data sources and checked against each other. We also exclude from the referencing procedure continuity constraints across adjacent tracks. Indeed, due to varying incidence angle, LOS velocity maps must be discontinuous across tracks. Continuity should then only be enforced after horizontal/vertical decomposition, or under the assumption of

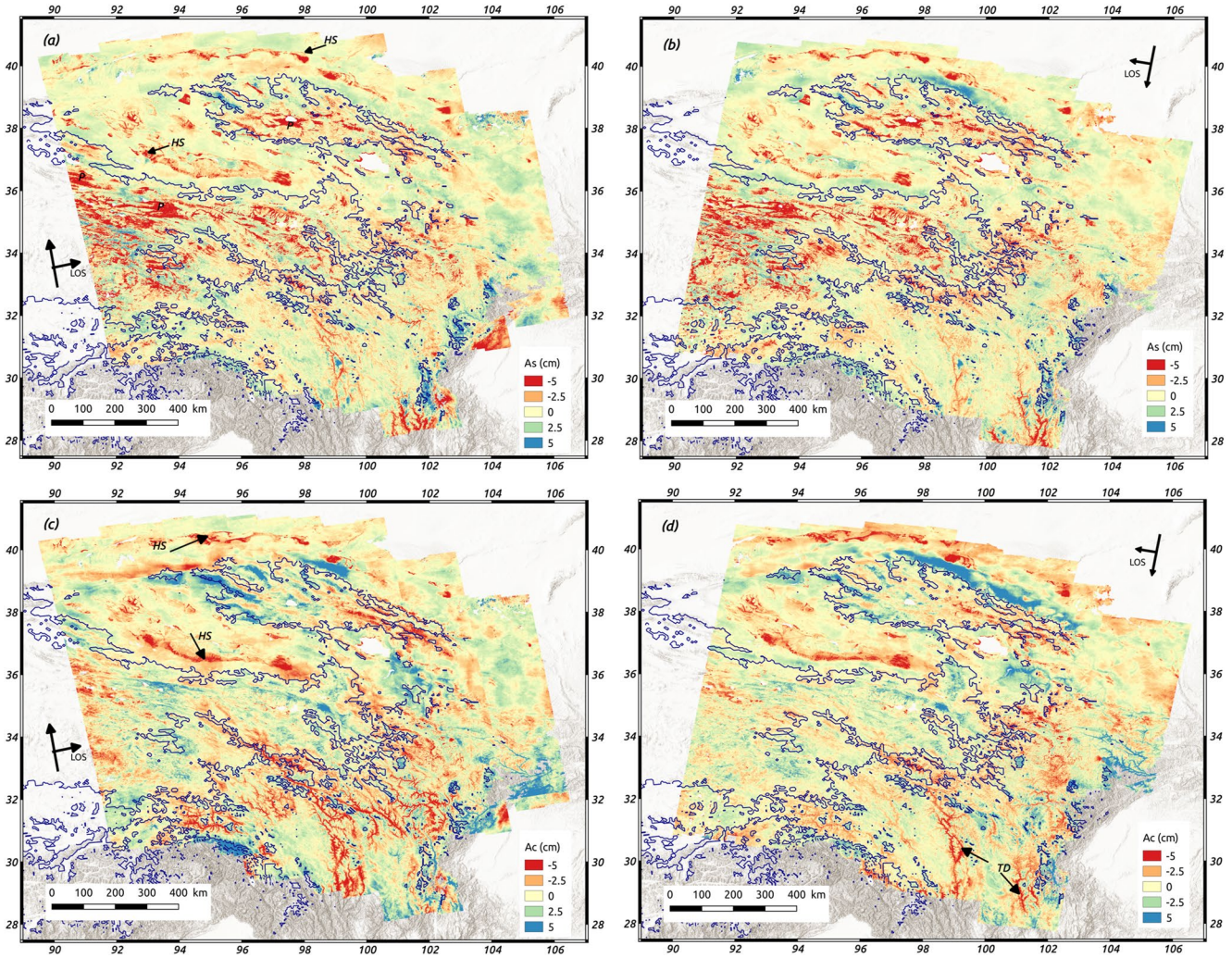

Figure 11. Amplitude of the seasonal signal extracted from time series analysis, superimposed on the elevation Shuttle Radar Topography Mission (SRTM). Dark blue lines contour permafrost-prone areas (T. Wang et al., 2020). Left: ascending tracks. Right: descending tracks. Panels (a–b): sine component. Positive (negative, respectively) amplitude indicates subsidence (uplift, respectively) in spring. Panels (c–d): cosine component. Positive (negative, respectively) values correspond to subsidence (uplift, respectively) in winter. "P" labels points toward examples of seasonal displacement induced by freeze-thaw cycles in the permafrost-prone area. "HS" labels show examples of hydrological signals. "TD" label points to examples of residual seasonal tropospheric delays in deeply incised valleys.

purely horizontal velocity. Here, we reference each track independently and use the redundancy on track overlaps to test the quality of the InSAR velocity maps at very large-scale.

We first assemble north to south segments (2 or 3) of each single track using the redundancy in their 150 km-long overlap areas, and obtain 7 ascending and 7 descending velocity maps. Then, we constrain a LOS velocity offset and a tilt in azimuth for each track, that is, we invert 2 free parameters for each ascending or descending tracks, that is, 28 parameters in total. We detail these two steps below (see also Figure 3 for a simplified view).

To assemble along-track segments, we first add to each velocity map (V_{LOS} from Equation 8) the ramp rates in range, $\dot{a} * x$, and in azimuth, $\dot{b} * y$, defined in subsections 3.2 and 3.3. We observe in the overlap regions that the difference of the velocity maps presents an offset and a slight ramp in range due to the fact that ramp rates in range are not evaluated exactly on the same data set for the different segments. The LOS velocity difference in overlap regions is thus fitted by a constant and a differential tilt in range, $\delta\dot{a}$. The $\delta\dot{a}$ value is split into $\delta\dot{a} = \delta\dot{a}^N - \delta\dot{a}^S$, where $\delta\dot{a}^N$ and $\delta\dot{a}^S$ are the tilt rate corrections for North and South segments, respectively. They are defined by the added weighting constraint: $\sigma_{\dot{a}} N \delta\dot{a}^N = -\sigma_{\dot{a}} S \delta\dot{a}^S$. The ramps $\delta\dot{a}^N x$ and $\delta\dot{a}^S x$ are then subtracted from the North and South velocity maps before merging. A similar method is used in the case of three along-track segments. At this step, we obtain merged LOS velocity maps with ramp rates added, but not yet referenced, $V_M(x, y)$.

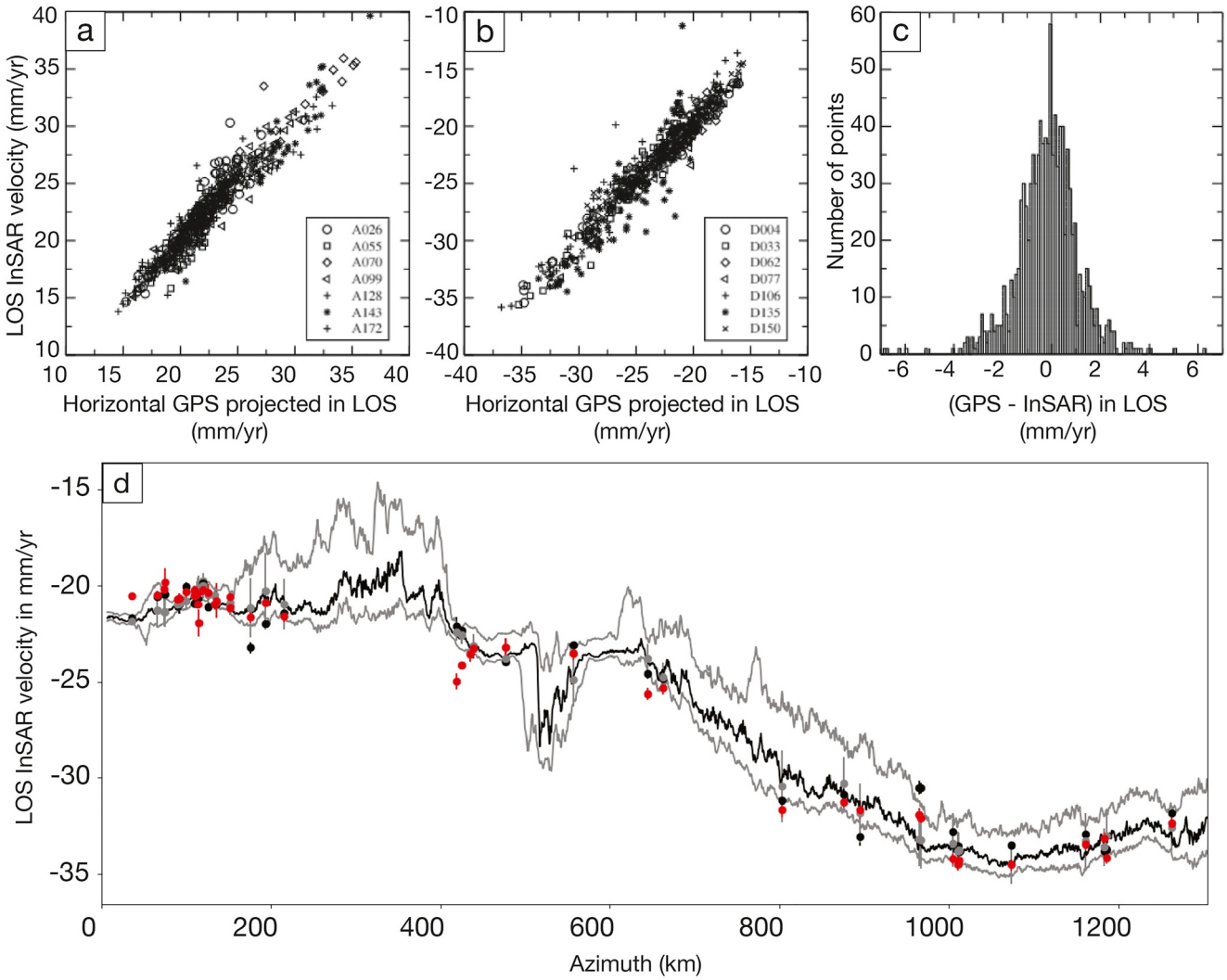

Figure 12. Comparison between the horizontal GNSS velocities from (M. Wang & Shen, 2020), projected in LOS, and the InSAR velocities after referencing in ITRF2008, (a) for ascending tracks. (b) For descending tracks. Note that track D135S presents larger errors due to 1.2 years of missing data in the South and a rugged and vegetated terrain. (c) Histogram of velocity differences. (d) Track-wide (250 km) InSAR profile along the azimuth of the merged and referenced D004 velocity map (see location in Figure S1 in Supporting Information S1). The effect of along range change in look angle, θ, is compensated by multiplying by $\sin\theta_{mid}/\sin\theta$, assuming a mainly horizontal velocity field (θ_{mid} is the middle look angle). The black line represents the median InSAR velocity value for each azimuth bin, after iterative outliers removal. The gray lines represent lateral variations in InSAR velocities, displayed as its mean plus or minus its standard deviation. Black filled circles (gray filled circles, respectively) show the mean (median, respectively) and standard deviation of InSAR velocities at GPS locations, in a small 1.0×2.7 km^2 area (in a larger 0.6×135 km^2 area, respectively). Filled red circles represent the horizontal GNSS velocities from M. Wang and Shen (2020) projected along LOS.

Horizontal GNSS data in ITRF2008 within the merged tracks are projected along the LOS and compared to the LOS InSAR velocity extracted at the same location. We compute the weighted mean of all velocity differences, V_c, after an iterative removal of the outliers. This mean is added to the LOS InSAR map, resulting in a preliminary referenced velocity map in ITRF, $V_{Refl}(x, y) = V_M(x, y) + V_c$. The velocity maps are then multiplied by $\sin\theta_{mid}/\sin\theta$, in order to take into account the effect of the incidence angle θ on horizontal motion (θ_{mid} is the middle incidence angle). This removes the range ramp due to incidence angle only, if one assumes horizontal motion. The flattened velocity map, $V_{RefI}^{flat}(x, y)$, has a reduced dispersion in the range direction. The same projection on θ_{mid} is done for GNSS velocities. A residual ramp in azimuth and an additional offset are then computed from the weighted residuals of GNSS LOS velocities minus their corresponding InSAR values. The offset, V_c', and ramp in azimuth, $\delta\dot{b}$, are added to the merged LOS InSAR maps using: $V_{RefF}(x, y) = V_M(x, y) + V_c + V_c' + \delta\dot{b} * y$. The resulting, final, referenced LOS velocity maps in the ITRF reference frame, $V_{RefF}(x, y)$, are shown in Figure S8 of Supporting Information S1, together with the GNSS velocities projected along LOS from M. Wang and

Shen (2020). An example of an azimuth profile of $V_{RefF}(x, y)$, multiplied by $\sin\theta_{mid}/\sin\theta$ to reduce the dispersion in range, is also shown in Figure 12d.

5.3. Referencing Validation by GNSS-InSAR Comparison in the Line of Sight

We compare here the horizontal GNSS data projected along the LOS to the velocities of the referenced InSAR maps (displayed in Figure S8 of Supporting Information S1). The comparison is shown in Figure 12 for ascending and descending tracks. The standard deviation of the LOS velocity difference is low, of 1.4 mm/yr, despite the very simple adjustment procedure described above. We adjust 28 free parameters (i.e., a ramp rate in azimuth $\delta\dot{b}$ and an offset V_c for each of the 14 tracks, Figure 3) for about 1,037 measurements of velocity differences. The absence of adjustment of range ramp in range and the simple tilt adjustment in azimuth over 1,200 km long tracks shows that multi-temporal InSAR analysis of Sentinel-1 data is able to retrieve very long wavelength surface deformation fields.

Note that in our referencing procedure, we neglect the vertical motion at GNSS locations. This does not imply that we will not be able to retrieve vertical motion even at large scale, as only the mean velocity value and azimuth tilt is fixed by horizontal GNSS data. Furthermore, we observe that GNSS data are almost all located on bedrock, hence are less subject to large vertical motion.

The main limitations to the simple referencing procedure described here are (a) the uneven sampling and data quality of GNSS data in general, and the sparse GNSS network in the westernmost part of the study area, (b) the period of observation, varying from site to site but long for GNSS data (up to 25 years), and short for InSAR (5 years), associated with a different sampling of the seismic cycle. In particular, the large-scale post-seismic signals from the 2001 Kokoxili earthquake and from the 2008 Wenchuan earthquake are clearly present in InSAR data but corrected in GNSS data, and may influence the referencing of the tracks covering the impacted areas. To partly overcome this problem, we imposed a low weight to InSAR-GNSS residuals close to the Kunlun fault.

5.4. InSAR Velocity Maps Decomposition Into Horizontal and Vertical Components

The referenced LOS velocity maps obtained above (Figure S8 in Supporting Information S1) are finally decomposed into horizontal and vertical components. The approach chosen here differs from other possible simplifications, as inverting for an E-W velocity and neglecting either the N-S velocity or the up-down contribution to the LOS InSAR measurements. Here, we fix the local azimuth of the horizontal velocity to the one obtained from the interpolated GNSS field (Figure S9 in Supporting Information S1). We invert for the horizontal, V_H, and vertical, V_U, velocities, with input data, V_{LOS}, on ascending and descending tracks, using equation:

$$V_{LOS} = (u_E * \sin(\alpha) + u_N * \cos(\alpha)) * V_H + u_U * V_U \quad (11)$$

where $u = (u_E, u_N, u_U)$ is the local unit LOS vector and α is the local azimuth of the horizontal velocity vector, counted clockwise from North. The system of Equation 11 is inverted where we have at least one ascending and one descending observation. The inverted values of V_H and the GNSS horizontal velocity amplitudes display overall good agreement, as shown on Figure 13a. This figure also highlights the high potential of InSAR data to spatially densify measurements of horizontal motion to complement GNSS, identify strain localization on and off-faults to further explore strain partitioning and slip transfer between faults over wide intracontinental deformation zones.

In areas where we have three or four observations, the absolute value of the residue of Equation 11 measures the consistency of overlapping velocity maps, while taking into account the viewing angle difference and the vertical motion. The residue is for 98% of pixels lower than 2 mm/yr (Figures 13b and 13d). In the diamond areas with four observations, the median of the residue is 1.2 mm/yr (Figures 13b and 13e). Note that here, we only constrain with InSAR the amplitude of the horizontal velocity vector, the angle of the velocity vector being fixed to the interpolated GNSS field. This resulting velocity vector has two components, with the northward component far less constrained than the eastward one. Residues in overlapping areas may also arise from local deviations of the velocity vector angle from the interpolated GNSS velocity angle.

The inverted horizontal velocities from InSAR differ from GNSS velocities by a standard deviation of 1.6 mm/yr (Figures 13b and 13c). The differences appear quite random in space with the notable exception of three main areas (redish dots in Figure 13b). In the southeasternmost part of our study area, at the limit of the Sichuan basin (between the Longriba fault and the LongmenShan thrust systems), InSAR yields a larger eastward velocity than GNSS, by about 3 mm/yr. This discrepancy must be due to the postseismic displacement associated with the Wenchuan 2008 Earthquake (M. Wang et al., 2021). In the western part of the velocity map around the

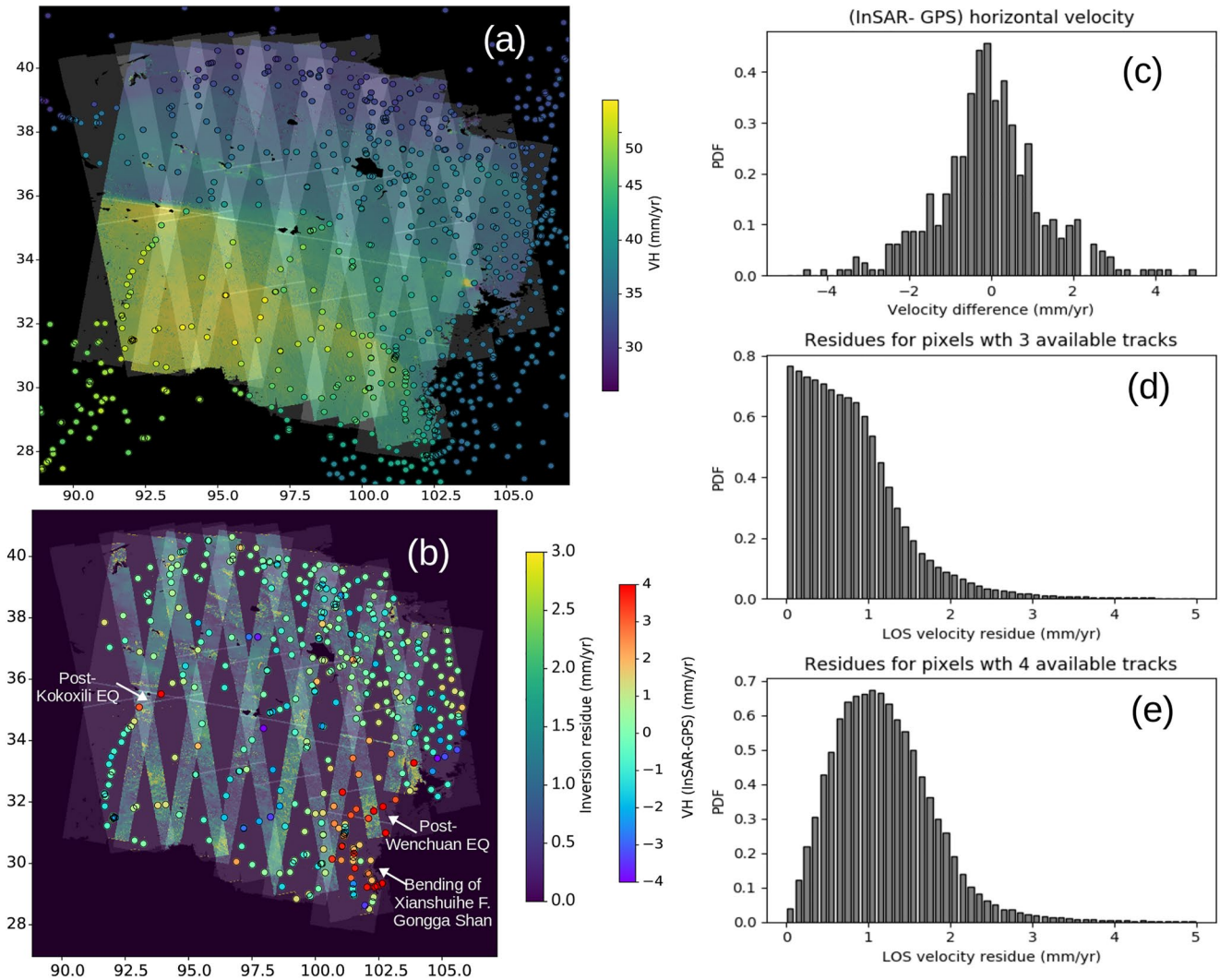

Figure 13. (a) Comparison of the amplitudes of the horizontal motion from GNSS (filled circles) and InSAR (color map). (b) Absolute residuals of the H-V decomposition on track overlaps (color strips) and signed GNSS-InSAR horizontal velocity difference (colored dots). Panels (a, b): the gray shade depicts the number of track available for each pixel. (c) Histogram of GNSS-InSAR horizontal velocity differences. (d) Distribution of the absolute residuals of the H-V decomposition where three tracks overlap. (e) As panel (c) but where four viewing angles are present (diamond shape areas).

Kunlun fault, we also observe the on-going post-seismic deformation after the 2001 Kokoxili earthquake (D. Zhao et al., 2021), leading to positive InSAR-GNSS residuals as this signal was corrected from the GNSS data (M. Wang & Shen, 2020). Finally, south of the eastern end of the XianShuiHe fault where it bends to the south, InSAR velocity maps yields higher velocity than long-term GNSS velocities, resulting in larger velocity contrasts across the fault by about 2–3 mm/yr. This may be due to the 3D complexity of the fault systems in this area, with the uplift of the Gongga Shan massif at the junction of the Xianshuihe Fault and a series of SW-NE thrusts as the Muli thrust (Bai et al., 2018; Pitard et al., 2021). Furthermore, this area is characterized by extreme relief with numerous deeply incised and vegetated valleys, which may induce InSAR measurements errors. It is also part of the southern segment of descending track D135 presenting a 1.2 years data gap, where we expect the automated MTInSAR processing to produce less accurate results than in the other parts of Tibetan plateau.

The horizontal and vertical velocity fields resulting from this analysis are displayed on Figure 14. Both show a good spatial across-track continuity, although this continuity was not enforced in the referencing procedure. We observe a north to south increase in horizontal velocities, with marked gradients across the Altyn Tagh, Haiyuan, Kunlun and Xianshuihe left-lateral fault systems. The velocity contrast across the Altyn Tagh is clearly visible up to 96°E, with a progressive eastward decrease and a relay to the Haiyuan fault, also marked by a velocity gradient

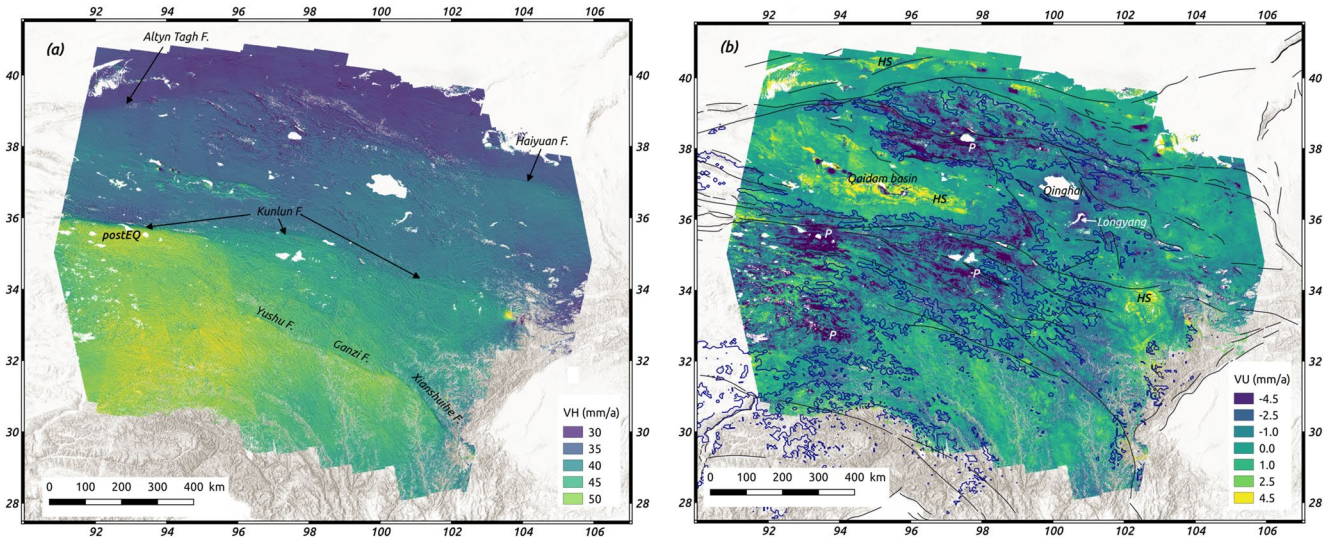

Figure 14. (a) Amplitude of the horizontal motion. Background shading is the gradient of the horizontal motion computed in a NNE direction. It underlines the major (labeled) faults mapped in Figure 1. The label "postEQ" is centered on the still ongoing postseismic deformation of the 2001 Kokoxili earthquake (b) Vertical velocity field (blue/yellow for subsidence/uplift). The dark blue lines show the limit of the permafrost domain from T. Wang et al. (2020). Faults are drawn with black lines. "P" stands for permafrost induced subsidence, "HS" for examples of hydrological uplift signals. We can see the subsidence signal induced by the lake level increase of Qinghai and Longyang lakes.

from 99° to 105.5°E. Strong localization on the Kunlun fault is visible throughout the study area, although velocity contrast decreases eastward. On the contrary the velocity contrast across the Xianshuihe fault vanishes westward, east of 96°E. The vertical velocity map appears to be dominated by hydrological contributions, with subsidence within permafrost-prone areas, and uplift in low elevation catchment basins. Although referencing is performed using only horizontal GNSS measurements, we show here that we can still retrieve a long-wavelength vertical velocity field, due to the small degree of freedom in our referencing procedure.

6. Discussion

6.1. Rationale for a Separate Analysis of Ramps

A specificity of our processing methodology is to separate the temporal inversion and analysis of the flattened interferograms from those of ramp measurements (Figure 3). Ramp rates are estimated on ramp time series and added back on velocity maps computed from flattened interferograms. The reasons are as follows:

- First of all, the orbit uncertainty and the ionospheric and residual tropospheric phase screens were believed to prevent multi-temporal InSAR analysis from reaching a few mm/yr accuracy on deformation at very large scales (e.g., Lanari et al., 2020; Parizzi et al., 2021), in contrast with what is expected when measuring small-scale deformation patterns. Therefore, one must first ascertain the confidence level that we have in ramp measurements, before possibly adding them back in velocity maps for further interpretation.
- Second, obtaining a velocity map from a linear regression through time of a phase time series affected by tilt oscillations is not ideal. The latter would appear as noise in time, and lead to a lower velocity amplitude by least-square regression than if these oscillations had previously been removed. Furthermore, the time series for some pixels may have data gaps due to areas that are not unwrapped, as could occur in the case of coherence drops due to snow or rain. In these noisy conditions, the best-fit velocity through the phase time series may be impacted by data holes in a non negligible way.
- Third, the weights applied for an optimized ramp inversion into time series (point 9 of subsection 2.2) are quite different than those used for time series inversion on each pixel. Similarly, the weights used for an optimized estimation of the ramp trends with time are different from those used for computing the velocity for each pixel (as in subsection 5.1). For example, the ramps obtained at the beginning of the time series must be strongly down-weighted.

We advocate that the separate analysis proposed here is necessary to reach the accuracy of about a mm/yr needed for large-scale tectonic studies.

6.2. Seasonal and Transient Signals

Ramp time series include seasonal and possibly transient ground displacement signals, which in theory could also be re-injected into the flattened time series. However, we must bear in mind that the ramps in range include a contribution due to the absolute value of the signal projected on varying look angles and a contribution from the gradient of the signal. The two effects cannot be disentangled in the absence of absolute measurements. In Tibet, we do not have access to seasonal GNSS data or GNSS time series to reference the absolute seasonal displacement. Therefore, re-introducing seasonal ramps in seasonal amplitude maps would introduce an ambiguity and offsets between adjacent tracks. Alternatively, focusing on the main hydrological origin of seasonal displacements, we chose to reference the seasonal terms in sine and cosine by setting to zero their average value over "bedrock" pixels in wide areas (more than 400×250 km^2), "bedrock" being defined as flat areas on sine amplitude maps. Furthermore, besides seasonal signals, we did not observe transient wide-scale deformation signals in Eastern Tibet during the 2015–2020 period. Therefore, here we only re-introduce ramp rates into velocity maps and discard the re-injection of seasonal or transient ramps into the displacement time series.

The origin of seasonal ramps must also be discussed. We did not attempt in this study to correct the ramp time series from atmospheric, hydrologic, or ocean tidal or non-tidal load effects. While the ocean tidal and non-tidal loading effect is low in Tibet (Yu et al., 2020), the seasonal ramp oscillations, evident for some tracks, could possibly result from the effect of seasonal hydrologic or atmospheric loading. The atmospheric load induces peak to peak, large-scale vertical displacement oscillations in our area of interest of about 3 mm on the plateau itself, increasing to 8 mm on its boundaries at lower elevation (Yan et al., 2019). Xiang et al. (2019) show that peak to peak seasonal vertical motion due to hydrologic loads in eastern Tibet, as derived from GNSS, GRACE or an hydrological model, presents a trend from about 15 mm in the south to about 4 mm in the north of our study area. They could produce seasonal ramps in range and/or azimuth of the order of 0.01 mm/km. Both effects could thus contribute to the seasonal signals observed in the ramp time series. However, the seasonal ramps observed here are quite large, around 0.05 mm/km. The seasonal geocenter motion could also contribute to the observed seasonal ramps. Here, we take them into account by an empirical adjustment with simple seasonal and semi-seasonal terms, in order to optimize the retrieval of the ramp rates. A correction based on hydrological and atmospheric loads could be tested in further studies, with the aim to improve the ramp rate estimation.

6.3. Residual Noise in Ramp Time Series

The residual ramps in range or azimuth are larger for ascending tracks acquired at dusk than for descending tracks acquired at dawn, suggesting a residual tropospheric or a ionospheric origin. The temporal variation in Total Electronic Content (TEC) generates a ramp in range due to varying look angles, whereas lateral TEC gradients will produce both a ramp in range and in azimuth, the latter yielding larger phase change for geometrical reasons. Azimuth ramps will also be large in case of very rapid temporal TEC dynamics. The standard deviation value found here for the residual ramps in azimuth, of 0.020 mm/km (0.029 mm/km, respectively) for descending (ascending, respectively) tracks corresponds very well to that found by Liang et al. (2019) for ionospheric ramps in Sentinel-1 in California, at similar mid geomagnetic latitude regions.

Part of this noise could have been mitigated by ionospheric corrections which were not attempted here. The split-spectrum method (Gomba et al., 2016) allows for retrieving Ionospheric Phase Screens (IPS) and correcting the phase time series. However, this powerful technique also strongly amplifies the impact of phase noise and of unwrapping errors in the IPS calculation. Thus, its use requires special caution, in our opinion not compatible with massive data processing. TEC corrections computed using Global Ionospheric Models (GIM), as given in S1 ETAD (Eineder et al., 2015) for example, could also be applied. However, available GIMs are still at low resolution (2.5 by 5 degrees, every hour), and their efficiency for correcting interferograms has yet to be quantified. For example, Yunjun et al. (2022) found that only the high resolution GIM from Jet Propulsion Laboratory (not freely available yet) significantly reduces the geolocation error of S1 ascending data in Chile.

We highlight ramp oscillations with periods of 24 days in ascending tracks only, thus with a possible ionospheric origin. We also observe that the residual ramps, during specific periods of the year, are in phase with tidal forces but not explained by SET. If the ionospheric origin of this signal were confirmed, it would suggest that efficient ionospheric corrections from TEC models should include the variability associated to possible amplifications of

ionospheric diurnal tides. Taking into account and correcting all non-stationary tidal signatures in the atmosphere could help to strongly reduce the noise standard deviations in InSAR ramps.

6.4. Ramp Rate Uncertainty

The ramps measured at the beginning of the time series appear noisier and were heavily down-weighted in the adjustment of Equation 1, before 2015.8 for descending tracks, and before 2016.8 for ascending tracks. Tentative explanations are that (a) the quality of the focusing and given metadata for early acquisitions is lower than for later acquisitions, (b) the orbits are less constrained, (c) the ramp in range induced by TEC is larger at the beginning of the time series. It is worth discussing these limits in more detail. First, the IPF software version used for focusing SAR data varies and our experience, also noted in Liang et al. (2019), is that we have more problems with wrong or less accurate annotations for the frequency modulation rates in early (2014–2015) acquisitions than later (2016 onward). Second, the precise orbits that were used in this study were computed with a time-varying methodology (Peter et al., 2021). For example, the gravity field employed by the CPOD team has changed at least three times. Finally, the ionospheric perturbations in InSAR S1 data decrease from year 2014 which is a maximum of solar activity to year 2018 which stands in a sunspot low (Liang et al., 2019).

Ramps rates measured in range might also be affected by a systematic bias. For example, a strong bias was observed due to an oscillator drift on the Envisat ASAR data (Marinkovic & Larsen, 2013). However, the S1 oscillator appears very stable (Larsen et al., 2017). A multi-annual TEC change or TEC gradient change could also produce a bias, which could be avoided with GIM-derived TEC corrections when validated (see subsection 6.3). In this study, the earliest ramp values are strongly down-weigthed and the time series is centered in an ionospheric low. We therefore neglect this potential bias source. Finally, an orbital drift with respect to the ITRF reference frame would produce a systematic deviation of ascending or descending ramp rates, with opposite signs. One may identify such a systematic deviation in Figure 10a, of about 0.002 mm/km/yr, equivalent to an E-W drift of approximately 2.5 mm/yr. However, this is far from being well resolved at this stage. A vertical movement of eastern Tibet as a whole would, in contrast, produce a deviation from the $y = x$ line in Figure 10a identical for the ascending or descending tracks.

A last point to discuss is the chosen realization of the ITRF reference frame to compare GNSS and InSAR data. In fact, the orbits used for our InSAR time series were computed in an ITRF reference frame evolving over time (ITRF 2008 until the end of 2016 then ITRF2014) (Peter et al., 2021). The GNSS velocity data from M. Wang and Shen (2020) is given in ITRF 2008. At this point, we think that the accuracy of the InSAR ramp rates does not allow an insightful discussion on the slight difference between the two reference frames in Tibet.

6.5. Vertical Velocity

Using only horizontal GNSS data to reference the LOS velocity maps leads us to assume a zero-mean and zero-tilt in azimuth for the vertical contributions on each track. Since the GNSS data are located in their vast majority on bedrock, they are only very moderately affected by permafrost, hydrology or gravitational instability. This can be verified with the good LOS GNSS-InSAR agreement seen on profiles, as the example shown in Figure 12d. Furthermore, outliers are detected and down-weighted in the InSAR-GNSS adjustment. As a result, these zero-mean and zero-tilt in azimuth constraints on the vertical contribution per track apply on bedrock. When the vertical velocity is computed from LOS and referenced velocity maps, these constraints imply that we cannot retrieve absolute or very large scale (more than 500 km) vertical displacement rates on bedrock.

Let us now discuss what would happen in case of an almost uniform uplift of eastern Tibet. A broad uplift pattern in Eastern Tibet has been measured by GNSS, varying from North to South from at most 3 mm/yr to about 1 mm/yr (Q. Zhao et al., 2023). It could produce a small ramp in azimuth of less than 0.0015 mm/yr/km, of opposite sign for ascending and descending data, which will be canceled by the ramp adjustment in azimuth. It can also lead to a small LOS ramp rate in range, due to varying look angles, of less than 0.002 mm/yr/km, positive toward the satellite for both ascending or descending data, in contrast to the effect of horizontal motion (see Figure 10). As the referencing only uses horizontal GNSS data, these ramps due to nearly uniform uplift should produce small discrepancies in the form of across-track discontinuities in the horizontal/vertical decomposition, and residues where we have more than two tracks available. Part of these discrepancies (totaling about 1 mm/yr and including other sources of errors) could thus be due to absolute or very large-scale vertical motion of Tibet.

6.6. Referencing Strategy

We use a very simple referencing procedure with few constraints from GNSS data. This allows to cross-check both data sets, extract a large-scale vertical motion not available on the GNSS data set, and to use overlap consistency for uncertainty measurements. The drawback however is that we do not ensure across-track continuity in horizontal or vertical motions.

Other referencing procedures published so far typically include the computation of a low-pass velocity field based on available GNSS data, that is then projected along LOS and removed from InSAR velocity maps (Tong et al., 2013). The corrected InSAR maps are high-pass filtered and the GNSS LOS velocity map is added back. Other related referencing method replace the high-pass filter step by a polynomial fit in both range and azimuth directions for each Sentinel-1 frame (250 km by 250 km) (Weiss et al., 2020). The advantage of these methods is that the long wavelength field is tied to external GNSS data, ensuring a good across-track and along-track continuity. However, the drawbacks, beside the lack of independence between the GNSS and InSAR velocity fields, are that high-pass filters are less efficient at frame borders, and more importantly, that the low-pass GNSS to InSAR tying might be impacted by local unsampled phenomena and by vertical motion. To clarify the latter point, we can consider the case of an area with no horizontal motion but with pervasive subsidence in numerous basins captured by InSAR. If GNSS points are mostly installed on bedrock, or if the GNSS vertical motion is either unavailable or unreliable, the GNSS interpolated surface will indicate zero motion in this area. The high-pass filtering of the InSAR minus the GNSS-derived surface will then show motion toward satellite on bedrock. Adding back GNSS-derived surface will leave this bias on InSAR velocity maps. Tiling of InSAR frames might then become hazardous. Such usual referencing procedures therefore only work well in the case of even, unbiased sampling of GNSS points, with coeval vertical rate measurements.

The present study still uses two degrees of freedom per track, adjusted using GNSS data, to reference the velocity maps. A next step would be to obtain absolute velocity measurements directly from SAR data. This requires obtaining the absolute InSAR phase. This problem is explored by Xu and Sandwell (2020), but still requires improvements in the geometric and atmospheric modeling of the satellite-to-ground delay before the absolute phase can be retrieved. Solving for the phase ambiguity can also be guided by range offset measurements, which provide an absolute measure of the satellite-to-ground delay. Yunjun et al. (2022) show that, after tropospheric, ionospheric (using the JPL high resolution global model and S1 topside ionospheric observations) and SET corrections, the standard deviation of the average range offset decreases to 5 cm. This remains yet too large for solving the 2.8 cm phase ambiguity, however this might be tackled by future studies.

7. Conclusion

The originality of this study is to explore to what extent MTInSAR based on Sentinel-1 acquisitions could be used for very large-scale mapping of surface displacements. In that end, we purposely limit the amount of free parameters needed for referencing InSAR data in the ITRF reference frame, so that we can then use the InSAR-GNSS independence to validate InSAR measurements. In all the studies we know of so far, this is the first time that such a strategy is experimented. The Tibetan plateau is a favorable study area to start with, due to its moderate relief, limited vegetation cover and high elevation, implying a thin tropospheric layer. It is also less affected by ionospheric disturbances than equatorial regions.

The data set, made of 7 ascending and 7 descending Sentinel-1 tracks over eastern Tibet, was processed automatically with the FLATSIM service (Thollard et al., 2021). The $\simeq$1,300 km-long tracks were divided in two or three chunks overlapping by about 150 km. To ensure high quality velocity maps, we post-processed all provided time series for each chunk, analyzing and taking into account measurement noise of diverse origins and a seasonal contribution.

The largest displacement wavelength that can be captured by MTInSAR corresponds to displacement tilts in azimuth and range. We show that it is useful to analyze them separately from the rest of the deformation signal. The quality of tilt observations is lower early in the time series than later. We show that InSAR is not only able to accurately measure the tilt in range due to solid earth tide, but it also measures the tilt in azimuth quite well. Furthermore, we show that other, time-dependent, lunar tidal effects of unknown origin, are apparent in the tilt time series. We suspect transient ionospheric tide amplifications, with high temporal dynamics, especially important for dawn orbits. The standard deviation of unmodelled, residual tilts for descending (ascending,

respectively) tracks is 0.042 mm/km (0.050 mm/km, respectively) in range direction and 0.020 mm/km (0.029 mm/km, respectively) in azimuth direction.

The careful ramp analysis allows to provide reliable estimates of the linear ramp evolution with time (ramp rate). We quantify their uncertainties for descending (ascending, respectively) tracks, at 0.0023 mm/km/yr (0.0030 mm/km/yr, respectively) in range direction, and 0.0011 mm/km/yr (0.0026 mm/km/yr, respectively) in azimuth direction. A comparison with the GNSS horizontal velocity data shows that the tilt rates accurately represent the plate motion in the ITRF 2008 reference frame, despite the changes made for orbit computation at the time of this study (Peter et al., 2021). No bias was observed neither for ascending nor descending tracks, although no ionospheric corrections were performed in this study. InSAR-GNSS tilt rates discrepancies are not only due to InSAR measurement errors at large wavelength, but also, and as importantly, to limitations such as uneven and possibly unrepresentative GNSS sampling, GNSS uncertainties, lack of GNSS vertical information, and differences in measurement periods in case of non linear motion.

Based on these first conclusions, we devise a very simple merging and referencing procedure. Tilt rates are reintroduced before along-track merging. Then a simple offset and final ramp adjustment in azimuth is performed for each track. Only two degrees of freedom are therefore used for each track. The adjustment is based on the GNSS-InSAR velocity differences at GNSS points, which avoids potential biases due to GNSS data interpolation and InSAR high-pass filtering. The measured misfit between the GNSS LOS-projected and InSAR LOS velocity maps is 1.4 mm/yr. It is again related not only to InSAR errors, but also to GNSS errors, lack of GNSS vertical velocity, and differences in sampling periods.

The horizontal-vertical decomposition allows to quantify the quality of the very large-scale InSAR maps. Indeed, tilted InSAR maps are used as input into the inversion to directly recover the horizontal velocity amplitude in the ITRF2008 reference frame. Wrong ramps would incorrectly attribute some horizontal motion to the vertical, or inversely, and that might be different from one track to the next. LOS residues ($\sigma = 1.2$ mm/yr) in regions of track overlaps allows to quantify the consistency of the LOS velocity maps while taking into account variable look angles. Horizontal GNSS-InSAR velocity differences have a standard deviation of 1.6 mm/yr.

Based on all the above quantified uncertainties, we show that it is possible to obtain InSAR velocity maps in the orbit reference frame, at very large scale, with little input from GNSS data. The obtained velocity and seasonal maps are rich in tectonic and hydrological signals, which will deserve more in-depth analysis in future studies.

Acknowledgments
Copernicus Sentinel-1 data, processed by ESA, have been accessed through the PEPS archive operated by CNES (https://peps.cnes.fr). MTInSAR processing was done on CNES HPC through the FLATSIM service operated jointly by INSU laboratories and CNES (ForM@Ter (2020): FLATSIM Data Products. CNES. (Dataset). doi: https://doi.org/10.24400/253171/FLATSIM2020). We thank the FLATSIM Team (Marie-Pierre Doin and Cécile Lasserre, Project Leaders, Catherine Proy, Project Manager, Michel Diament and P. Durand, Supervisors, Franck Thollard, Christophe Laurent, Erwan Pathier, Raphaël Grandin, Elisabeth Pointal, Emilie Deschamps-Ostanciaux, Dominique Clesse, project members) for building the FLATSIM service. Further reanalysis were performed on GRICAD computing environment from University Grenoble Alpes. CNES and the ESA-MOST Dragon 4 program supported the PhD fellowship of Laetitia Lemrabet. The work was also supported by the CNES APR project "TeraSAR-Tibet" and ANR project "Tibetan Orchestra." We thank the associate editor and the reviewers for their helpful comments. We thank Gilles Peltzer for fruitful discussions.

Data Availability Statement

The analysis presented here is based upon SAR Sentinel-1 data available https://peps.cnes.fr/rocket/#/home, and on GNSS data from Wang and Shen (2020) available at https://dataverse.harvard.edu/dataset.xhtml?persistentId=doi:10.7910/DVN/C1WE3N. Solid Earth tides have been computed with the Solid program from Dr. Dennis Milbert available at https://geodesyworld.github.io/SOFTS/solid.htm.

References

Altamimi, Z., Métivier, L., & Collilieux, X. (2012). ITRF2008 plate motion model. *Journal of Geophysical Research*, *117*(B7). https://doi.org/10.1029/2011JB008930

Aslan, G., Lasserre, C., Cakir, Z., Ergintav, S., Özarpaci, S., Dogan, U., et al. (2019). Shallow creep along the 1999 Izmit Earthquake rupture (Turkey) from GPS and high temporal resolution interferometric synthetic aperture radar data (2011–2017). *Journal of Geophysical Research: Solid Earth*, *124*(2), 2218–2236. https://doi.org/10.1029/2018jb017022

Bai, M., Chevalier, M.-L., Pan, J., Replumaz, A., Leloup, P. H., Métois, M., & Li, H. (2018). Southeastward increase of the late Quaternary slip-rate of the Xianshuihe fault, eastern Tibet. Geodynamic and seismic hazard implications. *Earth and Planetary Science Letters*, *485*, 19–31. https://doi.org/10.1016/j.epsl.2017.12.045

Bekaert, D. P., Karim, M., Linick, J. P., Hua, H., Sangha, S., Lucas, M., et al. (2019). Development of open-access standardized InSAR displacement products by the Advanced Rapid Imaging and Analysis (ARIA) project for natural hazards. In *AGU fall meeting abstracts* (Vol. 2019, p. G23A-04).

Biggs, J., Wright, T., Lu, Z., & Parsons, B. (2007). Multi-interferogram method for measuring interseismic deformation: Denali Fault, Alaska. *Geophysical Journal International*, *170*(3), 1165–1179. https://doi.org/10.1111/j.1365-246X.2007.03415.x

Brouwer, W. S., & Hanssen, R. F. (2021). An analysis of insar displacement vector decomposition fallacies and the strap-down solution. In *2021 IEEE International Geoscience and Remote Sensing Symposium IGARSS* (pp. 2927–2930). https://doi.org/10.1109/IGARSS47720.2021.9554216

Bürgmann, R., Schmidt, D., Nadeau, R. M., d'Alessio, M., Fielding, E. J., Manaker, D., et al. (2000). Earthquake potential along the Northern Hayward Fault, California. *Science*, *289*(5482), 1178–1182. https://doi.org/10.1126/science.289.5482.1178

Cavalié, O., Doin, M.-P., Lasserre, C., & Briole, P. (2007). Ground motion measurement in the Lake Mead area, Nevada, by differential synthetic aperture radar interferometry time series analysis: Probing the lithosphere rheological structure. *Journal of Geophysical Research*, *112*(B3), B03403. https://doi.org/10.1029/2006jb004344

Cavalié, O., & Jónsson, S. (2014). Block-like plate movements in eastern Anatolia observed by InSAR. *Geophysical Research Letters*, *41*(1), 26–31. https://doi.org/10.1002/2013GL058170

Cavalié, O., Lasserre, C., Doin, M.-P., Peltzer, G., Sun, J., Xu, X., & Shen, Z.-K. (2008). Measurement of interseismic strain across the Haiyuan fault (Gansu, China), by InSAR. *Earth and Planetary Science Letters*, *275*(3–4), 246–257. https://doi.org/10.1016/j.epsl.2008.07.057

Clark, M. K., & Royden, L. H. (2000). Topographic ooze: Building the eastern margin of Tibet by lower crustal flow. *Geology*, *28*(8), 703–706. https://doi.org/10.1130/0091-7613(2000)28⟨703:tobtem⟩2.0.co;2

Daout, S., Dini, B., Haeberli, W., Doin, M.-P., & Parsons, B. (2020). Ice loss in the Northeastern Tibetan Plateau permafrost as seen by 16 yr of ESA SAR missions. *Earth and Planetary Science Letters*, *545*, 116404. https://doi.org/10.1016/j.epsl.2020.116404

Daout, S., Doin, M.-P., Peltzer, G., Lasserre, C., Socquet, A., Volat, M., & Sudhaus, H. (2018). Strain partitioning and present-day fault kinematics in NW Tibet from Envisat SAR interferometry. *Journal of Geophysical Research: Solid Earth*, *123*(3), 2462–2483. https://doi.org/10.1002/2017jb015020

Daout, S., Doin, M.-P., Peltzer, G., Socquet, A., & Lasserre, C. (2017). Large-scale InSAR monitoring of permafrost freeze-thaw cycles on the Tibetan Plateau. *Geophysical Research Letters*, *44*(2), 901–909. https://doi.org/10.1002/2016gl070781

DiCaprio, C. J., & Simons, M. (2008). Importance of ocean tidal load corrections for differential InSAR. *Geophysical Research Letters*, *35*(22), L22309. https://doi.org/10.1029/2008GL035806

Doin, M.-P., Lasserre, C., Peltzer, G., Cavalié, O., & Doubre, C. (2009). Corrections of stratified tropospheric delays in SAR interferometry: Validation with global atmospheric models. *Journal of Applied Geophysics*, *69*(1), 35–50. https://doi.org/10.1016/j.jappgeo.2009.03.010

Doin, M.-P., Lodge, F., Guillaso, S., Jolivet, R., Lasserre, C., Ducret, G., et al. (2011). Presentation of the small Baseline NSBAS processing chain on a case example: The Etna deformation monitoring from 2003 to 2010 using Envisat data. In *Fringe Symposium*. Retrieved from https://hal-ens.archives-ouvertes.fr/hal-02185213

Doin, M.-P., Twardzik, C., Ducret, G., Lasserre, C., Guillaso, S., & Jianbao, S. (2015). InSAR measurement of the deformation around Siling Co Lake: Inferences on the lower crust viscosity in central Tibet. *Journal of Geophysical Research: Solid Earth*, *120*(7), 5290–5310. https://doi.org/10.1002/2014jb011768

Durand, V., Bouchon, M., Karabulut, H., Marsan, D., Schmittbuhl, J., Bouin, M.-P., et al. (2010). Seismic interaction and delayed triggering along the North Anatolian Fault. *Geophysical Research Letters*, *37*(18). https://doi.org/10.1029/2010GL044688

Eineder, M., Balss, U., Suchandt, S., Gisinger, C., Cong, X., & Runge, H. (2015). A definition of next-generation SAR products for geodetic applications. In *2015 IEEE International Geoscience and Remote Sensing Symposium (IGARSS)* (pp. 1638–1641). https://doi.org/10.1109/IGARSS.2015.7326099

England, P. C., & Jackson, J. (1989). Active deformation of the continents. *Annual Review of Earth and Planetary Sciences*, *17*(1), 197–226. https://doi.org/10.1146/annurev.ea.17.050189.001213

Farr, T. G., Rosen, P. A., Caro, E., Crippen, R., Duren, R., Hensley, S., et al. (2007). The shuttle radar topography mission. *Reviews of Geophysics*, *45*(2), 33. https://doi.org/10.1029/2005rg000183

Fattahi, H., Agram, P., & Simons, M. (2017). A network-based enhanced spectral diversity approach for TOPS time-series analysis. *IEEE Transactions on Geoscience and Remote Sensing*, *55*(2), 777–786. https://doi.org/10.1109/TGRS.2016.2614925

Fernández, M., Peter, H., Arnold, D., Duan, B., Simons, W., Wermuth, M., et al. (2022). Copernicus Sentinel–1 POD reprocessing campaign. *Advances in Space Research*, *70*(2), 249–267. https://doi.org/10.1016/j.asr.2022.04.036

Forbes, J. M., & Zhang, X. (2012). Lunar tide amplification during the January 2009 stratosphere warming event: Observations and theory. *Journal of Geophysical Research*, *117*(A12). https://doi.org/10.1029/2012ja017963

Gomba, G., Parizzi, A., De Zan, F., Eineder, M., & Bamler, R. (2016). Toward operational compensation of ionospheric effects in SAR interferograms: The split-spectrum method. *IEEE Transactions on Geoscience and Remote Sensing*, *54*(3), 1446–1461. https://doi.org/10.1109/TGRS.2015.2481079

Grandin, R. (2015). Interferometric processing of SLC Sentinel-1 TOPS data. In *Proceedings of fringe 2015: Advances in the Science and applications of SAR interferometry and Sentinel-1 InSAR Workshop*. European Space Agency. https://doi.org/10.5270/fringe2015.pp116

Grandin, R., Doin, M.-P., Bollinger, L., Pinel-Puyssegur, B., Ducret, G., Jolivet, R., & Sapkota, S. N. (2012). Long-term growth of the Himalaya inferred from interseismic InSAR measurement. *Geology*, *40*(12), 1059–1062. https://doi.org/10.1130/g33154.1

Grandin, R., Vallée, M., & Lacassin, R. (2017). Rupture process of the Mw 5.8 Pawnee, Oklahoma, earthquake from Sentinel-1 InSAR and seismological data. *Seismological Research Letters*, *88*(4), 994–1004. https://doi.org/10.1785/0220160226

Ho Tong Minh, D., Hanssen, R., Doin, M.-P., & Pathier, E. (2022). Advanced methods for time-series InSAR. In *Surface displacement measurement from remote sensing images* (pp. 125–153). John Wiley and Sons, Ltd. https://doi.org/10.1002/9781119986843.ch5

Hu, X., Bürgmann, R., Xu, X., Fielding, E., & Liu, Z. (2021). Machine-learning characterization of tectonic, hydrological and anthropogenic sources of active ground deformation in California. *Journal of Geophysical Research: Solid Earth*, *126*(11), e2021JB022373. https://doi.org/10.1029/2021jb022373

Hussain, E., Wright, T. J., Walters, R. J., Bekaert, D. P. S., Lloyd, R., & Hooper, A. (2018). Constant strain accumulation rate between major earthquakes on the North Anatolian Fault. *Nature Communications*, *9*(1), 1392. https://doi.org/10.1038/s41467-018-03739-2

Jolivet, R., Candela, T., Lasserre, C., Renard, F., Klinger, Y., & Doin, M.-P. (2015). The burst-like behavior of aseismic slip on a rough fault: The creeping section of the Haiyuan fault, China. *Bulletin of the Seismological Society of America*, *105*(1), 480–488. https://doi.org/10.1785/0120140237

Jolivet, R., Grandin, R., Lasserre, C., Doin, M.-P., & Peltzer, G. (2011). Systematic InSAR tropospheric phase delay corrections from global meteorological reanalysis data. *Geophysical Research Letters*, *38*(17). https://doi.org/10.1029/2011GL048757

Jolivet, R., Lasserre, C., Doin, M.-P., Guillaso, S., Peltzer, G., Dailu, R., et al. (2012). Shallow creep on the Haiyuan Fault (Gansu, China) revealed by SAR interferometry. *Journal of Geophysical Research*, *117*(B6). https://doi.org/10.1029/2011jb008732

Kohyama, T., & Wallace, J. M. (2014). Lunar gravitational atmospheric tide, surface to 50 km in a global, gridded data set. *Geophysical Research Letters*, *41*(23), 8660–8665. https://doi.org/10.1002/2014GL060818

Lanari, R., Bonano, M., Casu, F., Luca, C. D., Manunta, M., Manzo, M., et al. (2020). Automatic generation of Sentinel-1 continental scale DInSAR deformation time series through an extended P-SBAS processing pipeline in a cloud computing environment. *Remote Sensing*, *12*(18), 2961. https://doi.org/10.3390/rs12182961

Larsen, Y., Marinkovic, P., Dehls, J. F., Perski, Z., Hooper, A. J., & Wright, T. J. (2017). The Sentinel-1 constellation for InSAR applications: Experiences from the InSARAP project. In *2017 IEEE International Geoscience and Remote Sensing Symposium (IGARSS)* (pp. 5545–5548).

Lazecký, M., Spaans, K., González, P. J., Maghsoudi, Y., Morishita, Y., Albino, F., et al. (2020). LiCSAR: An automatic InSAR tool for measuring and monitoring tectonic and volcanic activity. *Remote Sensing*, *12*(15), 2430. https://doi.org/10.3390/rs12152430

Li, Y., Nocquet, J.-M., & Shan, X. (2022). Crustal deformation across the Western Altyn Tagh fault (86° E) from GPS and InSAR. *Geophysical Journal International*, *228*(2), 1361–1372. https://doi.org/10.1093/gji/ggab403

Liang, C., Agram, P., Simons, M., & Fielding, E. J. (2019). Ionospheric correction of InSAR time series analysis of C-band Sentinel-1 TOPS data. *IEEE Transactions on Geoscience and Remote Sensing*, *57*(9), 6755–6773. https://doi.org/10.1109/TGRS.2019.2908494

Liu, F., Elliott, J. R., Craig, T. J., Hooper, A., & Wright, T. J. (2021). Improving the resolving power of InSAR for earthquakes using time series: A case study in Iran. *Geophysical Research Letters*, *48*(14), e2021GL093043. https://doi.org/10.1029/2021GL093043

López-Quiroz, P., Doin, M.-P., Tupin, F., Briole, P., & Nicolas, J.-M. (2009). Time series analysis of Mexico City subsidence constrained by radar interferometry. *Journal of Applied Geophysics*, *69*(1), 1–15. https://doi.org/10.1016/j.jappgeo.2009.02.006

Marconato, L., Leloup, P., Lasserre, C., Jolivet, R., Caritg, S., Grandin, R., et al. (2022). Insights on fault reactivation during the 2019 November 11, M_w 4.9 Le Teil earthquake in southeastern France, from a joint 3-D geological model and InSAR time-series analysis. *Geophysical Journal International*, *229*(2), 758–775. https://doi.org/10.1093/gji/ggab498

Marinkovic, P., & Larsen, Y. (2013). Consequences of long-term ASAR local oscillator frequency decay - An empirical study of 10 years of data. In *FRINGE 2013 Workshop, 9-13 September 2013*.

Massonnet, D., Rossi, M., Carmona, C., Adragna, F., Peltzer, G., Feigl, K., & Rabaute, T. (1993). The displacement field of the Landers earthquake mapped by radar interferometry. *Nature*, *364*(6433), 138–142. https://doi.org/10.1038/364138a0

Mathey, M., Doin, M.-P., André, P., Walpersdorf, A., Baize, S., & Sue, C. (2022). Spatial heterogeneity of uplift pattern in the Western European Alps revealed by InSAR time-series analysis. *Geophysical Research Letters*, *49*(1). https://doi.org/10.1029/2021gl095744

Maubant, L., Pathier, E., Daout, S., Radiguet, M., Doin, M.-P., Kazachkina, E., et al. (2020). Independent component analysis and parametric approach for source separation in InSAR time series at regional scale: Application to the 2017–2018 slow slip event in Guerrero (Mexico). *Journal of Geophysical Research: Solid Earth*, *125*(3), e2019JB018187. https://doi.org/10.1029/2019jb018187

McCarthy, D. D., & Petit, G. (2004). IERS conventions (2003). *IERS Technical Note No. 32*.

Moore, C., Wright, T., & Hooper, A. (2021). Rift focusing and magmatism during late-stage rifting in Afar. *Journal of Geophysical Research: Solid Earth*, *126*(10), e2020JB021542. https://doi.org/10.1029/2020jb021542

Ou, Q., Daout, S., Weiss, J., Shen, L., Lazecký, M., Wright, T., & Parsons, B. (2022). Large-scale interseismic strain mapping of the NE Tibetan Plateau from Sentinel-1 interferometry. *Journal of Geophysical Research: Solid Earth*, *127*(6), e2022JB024176. https://doi.org/10.1029/2022jb024176

Parizzi, A., Brcic, R., & De Zan, F. (2021). InSAR performance for large-scale deformation measurement. *IEEE Transactions on Geoscience and Remote Sensing*, *59*(10), 8510–8520. https://doi.org/10.1109/TGRS.2020.3039006

Paulino, A. R., Araújo, F. D. S., Paulino, I., Wrasse, C. M., Lima, L. M., Batista, P. P., & Batista, I. S. (2021). Variability of the lunar semidiurnal tidal amplitudes in the ionosphere over Brazil. *Annales Geophysicae*, *39*(1), 151–164. https://doi.org/10.5194/angeo-39-151-2021

Pedatella, N., & Forbes, J. (2010). Global structure of the lunar tide in ionospheric total electron content. *Geophysical Research Letters*, *37*(6). https://doi.org/10.1029/2010gl042781

Peltzer, G., Rosen, P., Rogez, F., & Hudnut, K. (1996). Postseismic rebound in fault step-overs caused by pore fluid flow. *Science*, *273*(5279), 1202–1204. https://doi.org/10.1126/science.273.5279.1202

Peter, H., Fernández, M., Molina, J. B., & Fernández Sánchez, J. (2021). Copernicus Sentinel-1 satellites - Operational orbit determination at the Copernicus POD service. In *FRINGE 2017 Workshop, 31 May - 4 June 2021*.

Peter, H., Jäggi, A., Fernández, J., Escobar, D., Ayuga, F., Arnold, D., et al. (2017). Sentinel-1A – First precise orbit determination results. *Advances in Space Research*, *60*(5), 879–892. https://doi.org/10.1016/j.asr.2017.05.034

Pitard, P., Replumaz, A., Chevalier, M.-L., Leloup, P.-H., Bai, M., Doin, M.-P., et al. (2021). Exhumation history along the Muli thrust—Implication for crustal thickening mechanism in Eastern Tibet. *Geophysical Research Letters*, *48*(14), e2021GL093677. https://doi.org/10.1029/2021gl093677

Prats-Iraola, P., Scheiber, R., Marotti, L., Wollstadt, S., & Reigber, A. (2012). TOPS interferometry with TerraSAR-X. *IEEE Transactions on Geoscience and Remote Sensing*, *50*(8), 3179–3188. https://doi.org/10.1109/TGRS.2011.2178247

Stephenson, O. L., Liu, Y.-K., Yunjun, Z., Simons, M., Rosen, P., & Xu, X. (2022). The impact of plate motions on long-wavelength InSAR-derived velocity fields. *Geophysical Research Letters*, *49*(21). https://doi.org/10.1029/2022GL099835

Tapponnier, P., Lacassin, R., Leloup, P. H., Schärer, U., Dalai, Z., Haiwei, W., et al. (1990). The Ailao Shan/Red River metamorphic belt: Tertiary left-lateral shear between Indochina and South China. *Nature*, *343*(6257), 431–437. https://doi.org/10.1038/343431a0

Tapponnier, P., & Molnar, P. (1977). Active faulting and tectonics in China. *Journal of Geophysical Research*, *82*(20), 2905–2930. https://doi.org/10.1029/jb082i020p02905

Thollard, F., Clesse, D., Doin, M.-P., Donadieu, J., Durand, P., Grandin, R., et al. (2021). FLATSIM: The ForM@Ter LArge-scale multi-temporal Sentinel-1 InterferoMetry service. *Remote Sensing*, *13*(18), 3734. https://doi.org/10.3390/rs13183734

Tong, X., Sandwell, D., & Smith-Konter, B. (2013). High-resolution interseismic velocity data along the San Andreas Fault from GPS and InSAR. *Journal of Geophysical Research: Solid Earth*, *118*(1), 369–389. https://doi.org/10.1029/2012jb009442

Trubienko, O., Fleitout, L., Garaud, J.-D., & Vigny, C. (2013). Interpretation of interseismic deformations and the seismic cycle associated with large subduction earthquakes. *Tectonophysics*, *589*, 126–141. https://doi.org/10.1016/j.tecto.2012.12.027

Walters, R. J., Parsons, B., & Wright, T. J. (2014). Constraining crustal velocity fields with InSAR for Eastern Turkey: Limits to the block-like behavior of Eastern Anatolia. *Journal of Geophysical Research: Solid Earth*, *119*(6), 5215–5234. https://doi.org/10.1002/2013JB010909

Wang, H., & Wright, T. J. (2012). Satellite geodetic imaging reveals internal deformation of Western Tibet. *Geophysical Research Letters*, *39*(7). https://doi.org/10.1029/2012gl051222

Wang, M., & Shen, Z.-K. (2020). Present-day crustal deformation of continental China derived from GPS and its tectonic implications. *Journal of Geophysical Research: Solid Earth*, *125*(2). https://doi.org/10.1029/2019jb018774

Wang, M., Shen, Z.-K., Wang, Y.-Z., Bürgmann, R., Wang, F., Zhang, P.-Z., et al. (2021). Postseismic deformation of the 2008 Wenchuan earthquake illuminates lithospheric rheological structure and dynamics of Eastern Tibet. *Journal of Geophysical Research: Solid Earth*, *126*(9), e2021JB022399. https://doi.org/10.1029/2021JB022399

Wang, T., Yang, D., Yang, Y., Piao, S., Li, X., Cheng, G., & Fu, B. (2020). Permafrost thawing puts the frozen carbon at risk over the Tibetan Plateau. *Science Advances*, *6*(19). https://doi.org/10.1126/sciadv.aaz3513

Wei, M., Sandwell, D., & Smith-Konter, B. (2010). Optimal combination of InSAR and GPS for measuring interseismic crustal deformation. *Advances in Space Research*, *46*(2), 236–249. https://doi.org/10.1016/j.asr.2010.03.013

Weiss, J. R., Walters, R. J., Morishita, Y., Wright, T. J., Lazecky, M., Wang, H., et al. (2020). High-resolution surface velocities and strain for Anatolia from Sentinel-1 InSAR and GNSS data. *Geophysical Research Letters*, *47*(17). https://doi.org/10.1029/2020gl087376

Wright, T., Parsons, B., & Fielding, E. (2001). Measurement of interseismic strain accumulation across the North Anatolian Fault by satellite radar interferometry. *Geophysical Research Letters*, *28*(10), 2117–2120. https://doi.org/10.1029/2000gl012850

Xiang, Y., Yue, J., Bian, Y., Cai, D., & Cong, K. (2019). Seasonal crustal deformations around the Eastern Tibetan plateau constrained by GPS, GRACE and hydrological model. *Acta Geodynamica et Geomaterialia*, *16*, 429–440. https://doi.org/10.13168/agg.2019.0036

Xu, X., & Sandwell, D. T. (2020). Toward absolute phase change recovery with InSAR: Correcting for Earth tides and phase unwrapping Ambiguities. *IEEE Transactions on Geoscience and Remote Sensing*, *58*(1), 726–733. https://doi.org/10.1109/TGRS.2019.2940207

Yan, J., Dong, D., Bürgmann, R., Materna, K., Tan, W., Peng, Y., & Chen, J. (2019). Separation of sources of seasonal uplift in China using independent component analysis of GNSS time series. *Journal of Geophysical Research: Solid Earth*, *124*(11), 11951–11971. https://doi.org/10.1029/2019jb018139

Yu, C., Penna, N. T., & Li, Z. (2020). Ocean tide loading effects on InSAR observations over wide regions. *Geophysical Research Letters*, *47*(15), e2020GL088184. https://doi.org/10.1029/2020GL088184

Yunjun, Z., Fattahi, H., Pi, X., Rosen, P., Simons, M., Agram, P., & Aoki, Y. (2022). Range geolocation accuracy of C-/L-band SAR and its implications for operational stack coregistration. *IEEE Transactions on Geoscience and Remote Sensing*, *60*, 1–19. https://doi.org/10.1109/TGRS.2022.3168509

Zhao, D., Qu, C., Bürgmann, R., Gong, W., & Shan, X. (2021). Relaxation of Tibetan lower crust and afterslip driven by the 2001 Mw7. 8 Kokoxili, China, earthquake constrained by a decade of geodetic measurements. *Journal of Geophysical Research: Solid Earth*, *126*(4), e2020JB021314. https://doi.org/10.1029/2020jb021314

Zhao, Q., Chen, Q., van Dam, T., She, Y., & Wu, W. (2023). The vertical velocity field of the Tibetan Plateau and its surrounding areas derived from GPS and surface mass loading models. *Earth and Planetary Science Letters*, *609*, 118107. https://doi.org/10.1016/j.epsl.2023.118107